

Highlights

Implicit neural representations for accurate estimation of the standard model of white matter

Tom Hendriks, Gerrit Arends, Edwin Versteeg, Anna Vilanova, Maxime Chamberland, Chantal M.W. Tax

- Accurate and fast parameter estimation of the Standard model of white matter
- Create noise-robust continuous representations of diffusion MRI datasets
- No dependency on large training datasets due to the unsupervised neural network structure
- Easy incorporation of spatially varying acquisition protocols due to gradient non-uniformities

Implicit neural representations for accurate estimation of the standard model of white matter

Tom Hendriks^{a,1,*}, Gerrit Arends^{b,1}, Edwin Versteeg^b, Anna Vilanova^a, Maxime Chamberland^{a,2}, Chantal M.W. Tax^{b,c,2}

^aDepartment of Computer Science and Mathematics, Eindhoven University of Technology, Groene Loper 5, Eindhoven, 5612 AP, The Netherlands

^bCenter for Image Sciences, University Medical Center Utrecht, Heidelberglaan 100, Utrecht, 3584 CX, The Netherlands

^cCardiff University Brain Research Imaging Centre (CUBRIC), School of Physics and Astronomy, Cardiff University, Cardiff, United Kingdom

Abstract

Diffusion magnetic resonance imaging (dMRI) enables non-invasive investigation of tissue microstructure. The Standard Model (SM) of white matter aims to disentangle dMRI signal contributions from intra- and extra-axonal water compartments. However, due to the model's high-dimensional nature, extensive acquisition protocols with multiple b-values and diffusion tensor shapes are typically required to mitigate parameter degeneracies. Even then, accurate estimation remains challenging due to noise. This work introduces a novel estimation framework based on implicit neural representations (INRs), which incorporate spatial regularization through the sinusoidal encoding of the input coordinates. The INR method is evaluated on both synthetic and in vivo datasets and compared to parameter estimates using cubic polynomials, supervised neural networks, and nonlinear least squares. Results demonstrate superior accuracy of the INR method in estimating SM parameters, particularly in low signal-to-noise conditions. Additionally, spatial upsampling of the INR can represent the underlying dataset anatomically plausibly in a continuous way, which is unattainable with linear or cubic interpolation. The INR is fully unsupervised, eliminating the need for labeled training data. It achieves fast inference (~6 minutes), is robust to both Gaussian and Rician noise, supports joint estimation of SM kernel parameters and the fiber orientation distribution function with spherical harmonics orders up to at least 8 and non-negativity constraints, and accommodates spatially varying acquisition protocols caused by magnetic gradient non-uniformities. The combination of these properties along with the possibility to easily adapt the framework to other dMRI models, positions INRs as a potentially important tool for analyzing and interpreting diffusion MRI data.

Keywords: Diffusion MRI, Microstructure, Deep learning, Parameter estimation, Biophysical modeling, Quantitative MRI

*Corresponding author, email: t.hendriks@tue.nl

¹These authors contributed equally to this work.

²These authors contributed equally to this work.

1. Introduction

Diffusion magnetic resonance imaging (dMRI) is a non-invasive technique for in-vivo measurement of water diffusion in tissue using magnetic field gradients. To extract biologically interpretable information, a common approach is to fit a microstructural tissue model to a set of signals acquired with different dMRI acquisition settings (Alexander et al., 2019; Lampinen et al., 2023; Jelescu et al., 2020). In the absence of diffusion time dependence, these typically include different combinations of gradient strengths (commonly quantified by the b-value), directions (b-vector), and B-tensor shape (Westin et al., 2014). Microstructural parameters estimated by these models – including compartmental signal fractions and diffusivities – have shown to be sensitive to changes in brain structure due to diseases like multiple sclerosis (Alotaibi et al., 2021), Alzheimer disease (Parker et al., 2018) and Parkinson’s disease (Kim et al., 2016), and can provide a more fundamental understanding of tissue microstructure in both healthy and pathological tissues (Zhang et al., 2012).

The Standard Model of white matter (SM) (Novikov et al., 2019) describes the signal arising from white matter by a kernel consisting of three compartments (intra-axonal, extra-axonal, and free water (occasionally omitted)) convolved with a fiber orientation distribution (FOD) (Tournier et al., a). Compartmental signal fractions and diffusivities can be estimated, alongside the parameters that describe the FOD (usually in the form of a spherical harmonics (SH) series). Nevertheless, the high-dimensional parameter space of the SM complicates the estimation of its parameters, potentially leading to low accuracy, precision, and degeneracy of estimates (Jelescu et al., 2016). These issues become even more prominent at high noise levels.

Multiple strategies have been employed to fit microstructure models to dMRI data. When the primary goal is to estimate the tissue’s directional structure, a common two-step approach involves first fixing the kernel using a global estimate, followed by solving a linear inverse problem to estimate the fiber orientation distribution (FOD) (Tournier et al., 2007; Jeurissen et al., 2014). In contrast, when the focus is on estimating the kernel parameters, the orientational dependence is factored out by using rotational invariants of the signal (Novikov et al., 2018; Coelho et al., 2022; Reisert et al., 2017; Kaden et al., 2016). This last approach is most common for SM parameter estimation.

Estimation of SM parameters has been improved by machine-learning based methods including Bayesian estimators (Reisert et al., 2017), neural networks (de Almeida Martins et al., 2021; Diao and Jelescu, 2023), and fitting cubic polynomials (Coelho et al., 2022; Liao et al., 2024). Importantly, these approaches are commonly supervised machine-learning methods, operating at a voxel-level, that learn from large sets of existing data with a known ground truth – the training dataset. While this can be very effective, the quality of the results depend on biases existing in the training and inference datasets (Gyori et al., 2022). Additionally, since the methods operate at a voxel-level, they do not make any use of the spatial correlation that is naturally present in anatomy.

Recently, implicit neural representations (INRs) have been introduced to the dMRI domain as a novel fitting method. INRs have shown to create noise-robust continuous representations of dMRI datasets, using the spatial correlations present in the data. So far, they have been used to represent the diffusion signal using spherical harmonics basis functions and to estimate the parameters of (multi-shell multi-tissue) constrained spherical deconvolution (MSMT-CSD) (Hendriks et al., 2023; Consagra et al., 2024; Hendriks et al., 2025). In this previous work, INRs demonstrate potential to improve on voxel-based methods to estimate parameters, especially in more noisy or sparsely sampled datasets. Since INRs are spatially regularized continuous representations of the dataset, they can potentially be beneficial when performing downstream tasks which require interpolation, such as microstructure informed fiber tracking (Girard et al., 2017; Reisert et al., 2014).

In this work, we implement INRs for estimation of the SM and demonstrate the noise-robustness, continuous representation, and applicability of INRs for fitting on both synthetically generated and in vivo dMRI data. Synthetically generated datasets facilitate a quantitative analysis of the model outputs, while in vivo data quantitatively shows the performance in a realistic setting. The INR is compared to two existing machine learning methods (Coelho et al., 2022; de Almeida Martins et al., 2021) for fitting the SM, as well as nonlinear least squares. Additionally, moving beyond existing methods, the FOD SH coefficients up to order eight are estimated directly alongside the SM kernel parameters. Thus, in contrast to earlier methods that focused either on the kernel or on the FOD, this approach performs a joint estimation, which can improve accuracy and ameliorate degeneracy (Henriques et al., 2025). Moreover, because this is an unsupervised method, it does not rely on large training datasets as supervised methods do. It also does not require uniform acquisition parameters across voxels, making it capable of explicitly correcting for gradient non-uniformities (Bammer et al., 2003). The latter would become impractical for supervised methods which would

need prohibitively large sets of training data to capture voxel-wise protocol deviations. Altogether, the proposed method provides a flexible, noise-robust, spatially coherent way of fitting the SM, which is not biased by training data.

2. Methods

2.1. Standard model of white matter

Multiple approaches have been suggested to model white matter dMRI signal as a combination of sticks and anisotropic Gaussian diffusion compartments (Zhang et al., 2012; Reisert et al., 2017; Jespersen et al., 2007; Kroenke et al., 2004; Jelescu et al., 2016; Veraart et al., 2018; Fieremans et al., 2011). Generalization of this principle without introducing constraints on model parameters has led to a unified framework called the standard model of white matter (Novikov et al., 2018, 2019). The standard model assumes the measured signal S to be described by the convolution of a kernel $\mathcal{K}(b, b_\Delta, \mathbf{n} \cdot \mathbf{u})$ – describing the signal arising from water diffusing within and around a coherent fiber bundle with direction \mathbf{n} – with a distribution of fiber populations $\mathcal{P}(\mathbf{n})$

$$S(b, b_\Delta, \mathbf{u}) = S_0[\mathcal{K}(b, b_\Delta, \mathbf{n} \cdot \mathbf{u}) * \mathcal{P}(\mathbf{n})] \quad (1)$$

where b is the b-value, b_Δ is the b-tensor shape, \mathbf{u} describes the first eigenvector of the b-tensor, and S_0 is the signal without diffusion weighting. Our implementation of the SM assumes fiber bundles to consist of two compartments, intra-axonal and extra-axonal, that hold different diffusion characteristics. The signal from an axially symmetric tensor (zeppelin) compartment depends on its axial (D_{\parallel}) and perpendicular (D_{\perp}) diffusivity and is given by the following relation (Basser et al., 1994):

$$\begin{aligned} \mathcal{K}(b, b_\Delta, \mathbf{n} \cdot \mathbf{u}) = \exp\left(\frac{1}{3}bb_\Delta(D_{\parallel} - D_{\perp}) - \frac{1}{3}b(D_{\parallel} + 2D_{\perp}) \right. \\ \left. - bb_\Delta(\mathbf{n} \cdot \mathbf{u})^2(D_{\parallel} - D_{\perp})\right) \end{aligned} \quad (2)$$

The intra-axonal compartment is modeled as a zero-radius stick (i.e. $D_{\perp} = 0$) with $D_{\parallel} = D_i$, while the extra-axonal compartment is modeled as a zeppelin with axial and perpendicular diffusivity $D_{\parallel} = D_e$ and $D_{\perp} = D_p$, respectively. The fraction of the signal occupied by the intra-axonal compartment is given by f_i (thus setting the fraction of the extra-axonal compartment to $1 - f_i$). Summing over the intra-axonal and extra-axonal signal contributions, results in the following forward equation for the signal:

$$\begin{aligned} S(b, b_\Delta, \mathbf{u}) = S_0 \cdot \left[f_i \int_{|\mathbf{n}|=1} \exp(-b_\Delta(\mathbf{n} \cdot \mathbf{u})^2 D_i) \right. \\ \times \mathcal{P}(\mathbf{n}) d\mathbf{n} \cdot \exp\left(\frac{1}{3}bb_\Delta D_i - \frac{1}{3}b D_i\right) \\ + (1 - f_i) \int_{|\mathbf{n}|=1} \exp(-bb_\Delta(\mathbf{n} \cdot \mathbf{u})^2(D_e - D_p)) \\ \left. \times \mathcal{P}(\mathbf{n}) d\mathbf{n} \cdot \exp\left(\frac{1}{3}bb_\Delta(D_e - D_p) - \frac{1}{3}b(D_e + 2D_p)\right) \right]. \end{aligned} \quad (3)$$

Calculation of the integral can follow two approaches. The first approach leverages an analytical expression for the integral containing a product of Legendre polynomial function and an exponential term. This term arises when projecting $\mathcal{P}(\mathbf{n})$ on a SH basis. For a full derivation, see (Tax et al., 2021; Lampinen et al., 2020; Coelho et al., 2022). However, this analytical expression is only valid when $b_\Delta \geq 0$ and $D_e > D_p$ (see (Jespersen et al., 2007) for the derivation of this analytical solution). The second approach uses numerical integration to calculate the integral. This approach is able to incorporate negative b_Δ but is computationally more demanding than the analytical approach.

2.2. INR network architecture

The purpose of the INR is to map a coordinate vector \mathbf{x} to a desired output vector $\hat{\mathbf{k}}$ which represents the underlying dataset at that coordinate, by passing the coordinate through a neural network $\mathcal{F}_\Psi : \mathbf{x} \rightarrow \hat{\mathbf{k}}$ with weights Ψ . In our case we map a 3D-coordinate $\mathbf{x} \in \mathbb{R}^3$ to a vector of parameters for the SM kernel and FOD, $\hat{\mathbf{k}} = [D_i, D_e, D_p, f_i, S_0, p_0^0, \dots, p_l^m]$ where p_l^m is the coefficient of the SH basis function of order l and phase m . The signal is hence projected onto real SH as in (Lampinen et al., 2020). The implicit neural representation consists of three parts: the spatial encoding, a small multi-layer perceptron (MLP), and a number of output layers (Figure 1). Each of the parts will be discussed in-depth in the upcoming sections.

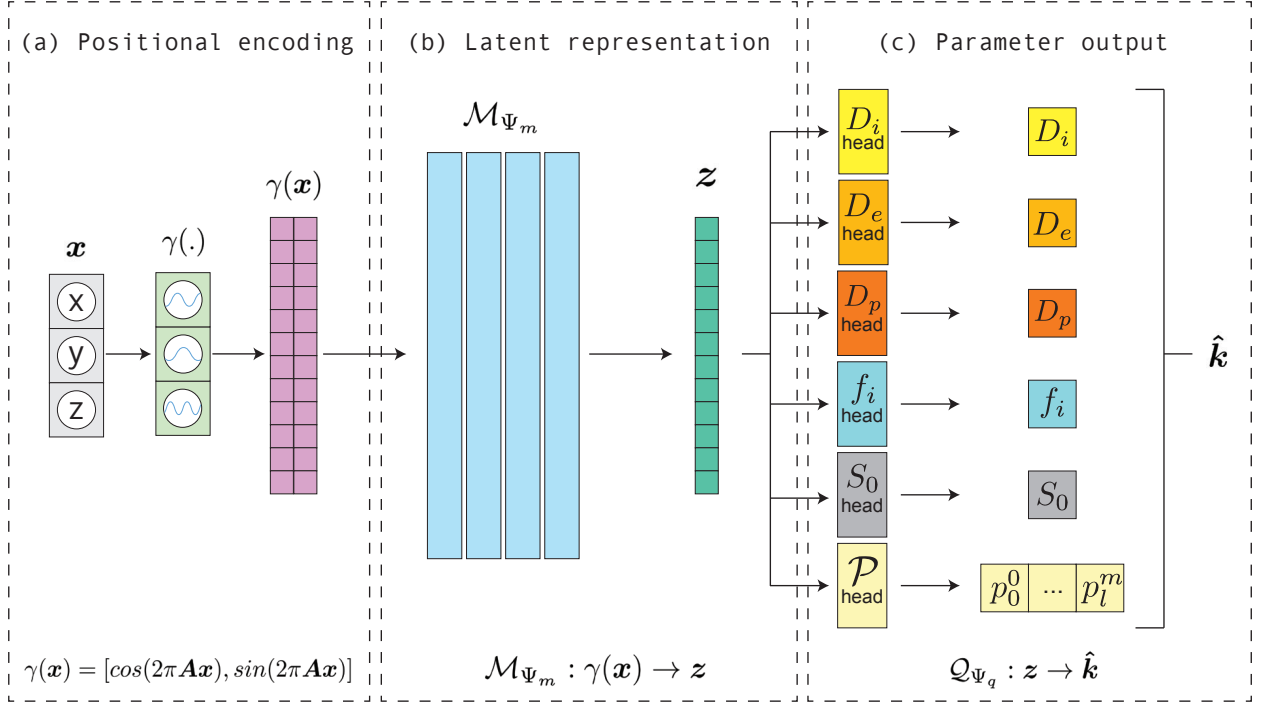


Figure 1: INR network architecture. **a)** shows how the input (signal + coordinates) is mapped to a higher dimensional frequency space. **b)** These values are then forwarded to the MLP. **c)** Output layer of the MLP is converted to SM parameters.

2.2.1. Spatial encoding

By encoding the input coordinates to a high dimensional space before entering them into the model, we can greatly increase the representational power of the INR (Tancik et al., 2020). We use the Fourier features encoding described by Tancik et al. (Tancik et al., 2020), which was used previously to model MSMT-CSD using INRs (Hendriks et al., 2025). First we scale the coordinates \mathbf{x} (maintaining aspect ratio) to lie in range $[-1, 1]^3$, and then apply to following transformation

$$\gamma(\mathbf{x}) = [\cos(2\pi\mathbf{A}\mathbf{x}), \sin(2\pi\mathbf{A}\mathbf{x})] \quad (4)$$

where $\gamma(\cdot)$ is the Fourier feature encoding, and \mathbf{A} is a size $n_p \times 3$ matrix with values sampled from $\mathcal{N}(0, \sigma^2)$. The number of encodings n_p and the standard deviation σ^2 are hyperparameters that can be adapted to suit datasets of varying complexity and quality. This process results in an encoded coordinate vector $\gamma(\mathbf{x}) \in [-1, 1]^{n_p \times 2}$.

2.2.2. Multi-layer perceptron

The MLP \mathcal{M}_{Ψ_m} with weights Ψ_m (m pointing towards corresponding MLP) is the backbone of INR and is largely responsible for representing the underlying dataset. It consists of four fully-connected layers of equal sizes n_h , determined by the complexity of the represented dataset, and ReLU activation functions. The MLP maps the encoded coordinates to some latent vector $\mathcal{M}_{\Psi_m} : \gamma(\mathbf{x}) \rightarrow \mathbf{z}$ with $\mathbf{z} \in \mathbb{R}_+^{n_h}$, that serves as an input to the output layers.

2.2.3. Output layers

The final part of the INR architecture maps \mathbf{z} to a parameter estimate $\hat{\mathbf{k}}$ using a separate fully connected layer, called 'head', for each parameter estimate. For the SM parameters \hat{D}_i , \hat{D}_e , \hat{D}_p , and \hat{f}_i the heads use a Sigmoid activation function scaled to fit physiological ranges (Table 1). For \hat{S}_0 a softplus activation function which ensures positivity, without an upper bound (Dugas et al., 2000). The SH-coefficients of the estimated FOD $\hat{\mathcal{P}}(\mathbf{n})$ require both positive and negative outputs and, therefore, have no activation function. This results in the full output layer of the INR providing the mapping $\mathcal{Q}_{\Psi_q} : \mathbf{z} \rightarrow \hat{\mathbf{k}}$ where \mathcal{Q}_{Ψ_q} are the output layers with weights Ψ_q .

	D_i	D_e	D_p	f_i	S_0
min.	0	0	0	0	0
max.	4	4	1.5	1	-

Table 1: Table showing the lower (min.) and upper (max.) bounds of the estimated parameters, diffusivities shown in $\mu\text{m}^2/\text{ms}$.

2.3. Model fitting

Given set of N_m (capital N denoting a fixed number, opposed to lower case hyperparameters n_p and n_h) measurements $\{(b_i, (b_\Delta)_i, \mathbf{u}_i) | i \in 1, \dots, N_m\}$, measured at coordinates $\mathbf{x}_j \in \mathbf{X}$ with $\mathbf{X} \subset \mathbb{R}^3$ being the set of all measured coordinates in the dMRI dataset, the estimated signal $\hat{S}(b_i, (b_\Delta)_i, \mathbf{u}_i, \mathbf{x}_j)$ at coordinate \mathbf{x}_j is obtained from the model output $\mathcal{F}_\Psi : \mathbf{x} \rightarrow \hat{\mathbf{k}}$ by calculating the estimated kernel $\hat{\mathcal{K}}(b, b_\Delta, \mathbf{n} \cdot \mathbf{u})$ using (2) and convolving with $\hat{\mathcal{P}}(\mathbf{n})$ as in (1). We approximate the desired INR \mathcal{F}_Ψ with weights $\Psi := \{\Psi_m, \Psi_q\}$ by finding the weights Ψ^* that minimize the error (mean squared error (MSE) or Rician likelihood loss (Parker et al., 2023), the latter allowing an explicit correction of Rician noise) between the estimated signal \hat{S} and the measured signal S

$$\Psi^* = \underset{\Psi}{\operatorname{argmin}} \frac{1}{|\mathbf{X}|} \sum_{\mathbf{x}_j \in \mathbf{X}} \sum_{i=1}^{N_m} \mathcal{L}(S(b_i, (b_\Delta)_i, \mathbf{u}_i, \mathbf{x}_j), \hat{S}(b_i, (b_\Delta)_i, \mathbf{u}_i, \mathbf{x}_j)) + \Lambda_{\mathbf{x}_j} \quad (5)$$

where \mathcal{L} is either the MSE or the Rician likelihood loss. We include an additional term $\Lambda_{\mathbf{x}_j}$ which is a non-negativity constraint for the FOD at \mathbf{x}_j , as described by Tournier et al. (Tournier et al., a). The constraint is calculated by sampling the FOD across the spherical domain and adding any negative values as a loss. The fitting process is shown in Figure 2.

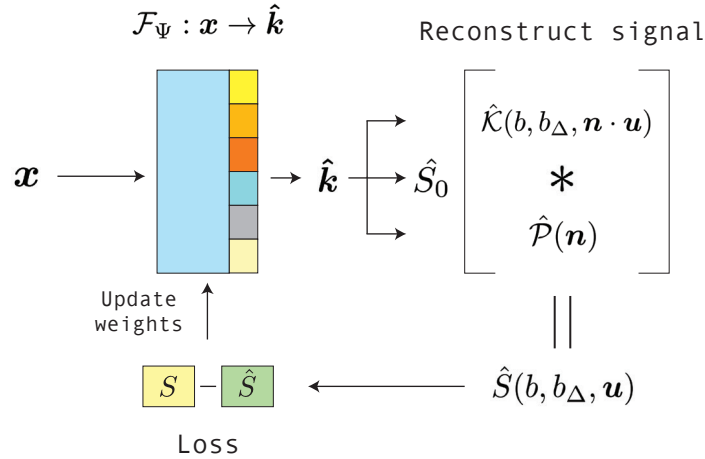


Figure 2: Visualization of the INR fitting process. The input coordinates \mathbf{x} are input in the INR (architecture shown in Figure 1) and are mapped to a parameter estimate $\hat{\mathbf{k}}$. Using $\hat{\mathbf{k}}$ the signal estimate \hat{S} is reconstructed following (3). The loss between \hat{S} and the measured signal S is used to update the INR weights.

2.4. Implementation

The INR is implemented in Python 3.10.10 using PyTorch 2.0.0. An Adam optimizer was used with a learning rate of 10^{-4} and default settings otherwise. The hyperparameters were set at $n_p = 5000$, $n_h = 2048$, $\sigma^2 = 3.5$ for the SNR 50 synthetic datasets (see section 2.6) and the in-vivo dataset (see section 2.7), and $\sigma^2 = 2.5$ for the SNR 20 synthetic datasets. More details about the choice of σ^2 is given in Appendix A. Each INR was fit for 150 epochs on an NVIDIA RTX 4080 GPU with 16GB of VRAM, with a batch size of 500. Visualizations of the model output were created using matplotlib 3.8.0, and MRtrix3 3.0.4 (Tournier et al., b). Numerical integration to calculate the integral during training is implemented with Torchquad Simpson function (Gómez et al., 2021).

2.5. Comparisons

The performance of the INR model (referred to as the INR method) is compared to three other SM model fitting methods described below. A supervised machine learning approach using the SMI toolbox (Coelho et al., 2022) (SMI method) with standard settings. The SMI method requires a noise map, which was determined using MP-PCA denoising (Veraart et al., 2016). A supervised deep learning method (referred to as the supervised NN method introduced in (de Almeida Martins et al., 2021)) was trained using a combination of synthetic and data-driven parameter samples. Specifically, the training data consisted of 500,000 samples, with 75% allocated for training and 25% for validation. Half of the training samples were generated by uniformly sampling model parameters, while the other half were derived by applying mutations to nonlinear least squares (NLLS) estimates obtained from the target dMRI data. The neural network architecture comprised three hidden layers with 150, 80, and 55 neurons. Gaussian noise was added with signal to noise ratio (SNR) 50. For a comprehensive description of all training settings, see (de Almeida Martins et al., 2021). Finally, a NLLS approach (NLLS method) was implemented with the MATLAB (MathWorks, Natick, MA, USA) optimization toolbox: lsqnonlin with Levenberg-Marquardt algorithm, max 1000 iterations.

Of the above methods, only INR has a positivity constraint implemented for the FOD (see section 2.3).

Fitting performance across the different methods was evaluated using the Pearson correlation coefficient (ρ) and the Root Mean Squared Error (RMSE) on kernel parameters and rotational invariant $p_2 = \sqrt{\frac{4\pi}{5}} \sqrt{\sum_m |p_{2m}|^2}$, where $|p_{2m}|^2$ is the absolute value of the second order, m-th phase SH coefficient.

2.6. Generation of simulated ground truth data

In silico experiments were conducted on simulated data obtained from one brain (subject 011) of the MGH Connectome Diffusion Microstructure Dataset (Tian et al., 2022a). The dMRI data were acquired on the 3T Connectome MRI scanner (Magnetom CONNECTOM, Siemens Healthineers). The acquisitions with $b = [0, 50, 350, 800, 1500, 2400, 3450, 4750, 6000]$ s/mm² and $\Delta = 19$ ms were selected. The lowest 4 b-values were acquired with 32 uniformly distributed diffusion encoding directions, the highest 4 b-values with 64. The dataset also contained 50 b=0s/mm² volumes. More details about the imaging parameters and processing can be found in (Tian et al., 2022b). The SM was fitted with the SMI toolbox (Coelho et al., 2022) to generate a set of realistic SM kernel parameters for f_i , D_i , D_e , and D_p , using $l_{max} = 4$ and noise bias correction with a sigma map acquired through MP-PCA (Veraart et al., 2016). To enhance the smoothness of the kernel maps, anisotropic diffusion filtering was performed using MATLAB's imdiffusefilt function with three iterations (N=3) and minimal connectivity. The SH coefficients p_{lm} of the FOD were calculated using Multi-Shell Multi-Tissue Constrained Spherical Deconvolution (MSMT CSD) (Jeurissen et al., 2014) for $l_{max} = [2, 4, 6, 8]$. The simulated signals corresponding to these parameters were calculated from the SM signal equation with a published optimized acquisition protocol (Coelho et al., 2022): $b = [0, 1000, 2000, 8000, 5000, 2000]$ s/mm², number of directions [4, 20, 40, 35, 15], and B-tensor shape $b_\Delta = [1, 1, 1, 1, 0.8, 0]$. Directions were optimized by minimization of the electric potential energy on a hemisphere (Garyfallidis et al., 2014) after which half of the directions were flipped. Finally, Gaussian noise was added. The standard deviation of the noise distribution was determined by the mean of the b=0s/mm² acquisitions and the SNR (20,50 or ∞), resulting in a spatially varying standard deviation. Free water contributions and TE dependence were not considered. Non-white matter voxels are masked out as their influence on the loss value will decrease the performance of parameter estimation on white matter voxels. A white matter mask was generated with the Freesurfer (Fischl, 2012) segmentation which is included in the MGH dataset. Voxels with $D_e > D_p$ were also masked out as these represent nonphysical behavior.

Table 2: In vivo diffusion acquisition scheme and imaging parameters.

b_{Δ}	b-value [s/mm²]											
	0	100	200	700	1300	1450	1800	2400	2700	2750	3000	4000
0	2	6	x	6	6	x	6	6	x	x	6	x
-0.5	1	x	3	x	x	10	x	x	3	20	x	42
0.5	1	x	3	x	x	10	x	x	3	20	x	42
1	2	x	6	x	x	20	x	x	6	40	x	84

Parameter	Value
Echo Time TE [ms]	77
Repetition time TR [ms]	2800
Voxel size [mm ³]	3 × 3 × 3
Field-of-view [mm ³]	210 × 210 × 45
Time between diffusion gradients [ms]	7.4
Diffusion gradient duration [ms]	30 + 24
Acceleration	Partial Fourier 6/8

2.7. In vivo data acquisition

The study was approved by the Cardiff University School of Psychology Ethics Committee and written informed consent was obtained from the participant in the study. One healthy volunteer was scanned on a 3T, 300 mT/m Connectom scanner (Siemens Healthineers, Erlangen, Germany). Imaging parameters and diffusion acquisition scheme can be found in Table 2. Gradient waveforms for spherical tensor encoding were optimized using the NOW toolbox (Sjölund et al., 2015).

2.8. Experiments

2.8.1. Experiment 1: Quantitative comparison on simulated data

All four fitting methods were compared on simulated data. To mimic realistic conditions, Gaussian noise was added during the simulation of the synthetic dataset (SNR = [20,50]). For this experiment, only $l_{max} = 2$ was considered, which is the highest SH order the supervised NN method can fit. As the used optimized acquisition protocol contains only positive b_{Δ} values, the SM forward model was calculated following the analytical approach.

2.8.2. Experiment 2: Rician noise bias

The effect of Rician noise bias was investigated by introducing noise sampled from a Rician distribution (SNR = [20,50]), rather than Gaussian. Parameter estimation was performed using both a standard MSE loss and a Rician likelihood loss (Parker et al., 2023), and the resulting estimations were compared to the ground truth. The integral in the SM forward model is calculated with the analytical approach.

2.8.3. Experiment 3: Qualitative comparison on in vivo data

To test the INR on in vivo data, SM parameter estimation was executed on the dataset from section 2.7. Only $l_{max} = 2$ was considered. As the acquisition protocol contained negative b_{Δ} values, the SM forward model was calculated following the numerical integration approach. The results are compared to the estimates from the methods in section 2.5.

2.8.4. Experiment 4: Estimation of SH order up to $l_{max} = 8$

The performance of the proposed method to model higher order FODs is investigated by fitting the INR with SH orders of $l_{max} = \{2, 4, 6, 8\}$, for three different datasets. The noiseless synthetic dataset and the SNR 50 synthetic data provide insight in the accuracy of FOD estimation in noisy data, while the in vivo dataset qualitatively evaluates the capability to estimate higher order FODs on realistic datasets.

2.8.5. Experiment 5: Effect of gradient non-uniformity correction of SM parameter estimation

The impact of gradient non-uniformities on SM parameter estimation was assessed using in vivo data. For each voxel, the b-value, b_Δ , and b-vectors were recalculated to account for scanner-specific gradient deviations following (Bammer et al., 2003). These corrected diffusion parameters were then incorporated into the training loop by providing them as additional inputs to the data loader. This analysis was performed for $l_{max} = 2$. The differences between the corrected and uncorrected parameter estimates were subsequently evaluated. Gradient non-uniformity correction was implemented using both MSE and Rician loss functions.

2.8.6. Experiment 6: Implicit neural representation for spatial interpolation

To obtain more detailed insight into the continuous spatial representation of the dataset provided by an INR, the INR fit on the Gaussian noise, SNR 50 synthetic dataset at $l_{max} = 2$ is sampled at 8x the original resolution in every dimension, resulting in 0.375mm isotropic voxels. The parameter map of p_2 was visualized in the coronal and sagittal plane for the original resolution output of the model and the linear, cubic and INR upsampling.

3. Results

3.1. Quantitative comparison on simulated data

Results from experiment 1 are presented in Fig. 3 (SNR = 20). When Gaussian noise is added, the INR method shows superior performance for all SM parameters, with both ρ and RMSE achieving the highest values. Brain parameter maps from Fig. 3b shows the ability of the INR method to reproduce smooth parameter maps similar to the ground truth, where the voxel-wise fitting methods show noisy estimates due to the lack of spatial regularization. The INR method does exhibit minor overestimation of D_e in the splenium of the corpus callosum compared to the ground truth.

Parameter estimation on simulated data without noise and with SNR = 50 can be found in Appendix B, showing a less prominent, but still evident improvement in ρ and RMSE of the INR method compared to other estimation methods for all parameters. Fitting without noise shows that the ground truth generating process is not positively biased towards parameter estimates of the INR.

3.2. Rician noise bias

The correlation plots between the INR with MSE or Rician loss and the ground truth parameters, alongside the parameter maps for both approaches can be seen in Figure 4. For MSE, the Rician bias is visible in the scatterplots and parameter maps as a general over- or underestimation across all voxels. The Rician loss is able to correct the bias, resulting in better correlation with the ground truth. The bias is most significant for D_i and D_e . The bias effect is less prominent when considering SNR = 50, see supplementary information Fig. C.12.

3.3. Qualitative comparison on in vivo data

The parameter maps for the in vivo dataset for the different methods are seen in Figure 5. The differences between methods are especially visible in the capsula interna and externa, and the splenium of the corpus callosum. The INR produces maps that are more spatially smooth and show a clear (and anatomically plausible) structure, while other methods display higher spatial variability.

3.4. Estimation of SH order up to $l_{max} = 8$

The INR outputs for the different SH order FODs are visualized in Figure 6. Qualitative inspection of the FODs shows plausible FOD shapes and directions throughout all datasets and SH orders. Furthermore, there are no notable differences between the FOD estimates for the clean and noisy synthetic datasets, indicating noise robustness in the estimate. The backgrounds in Figure 6 show no large voxel-wise differences for f_i across the different orders. This holds true for all kernel parameter estimates, which is shown in further detail in Appendix D.

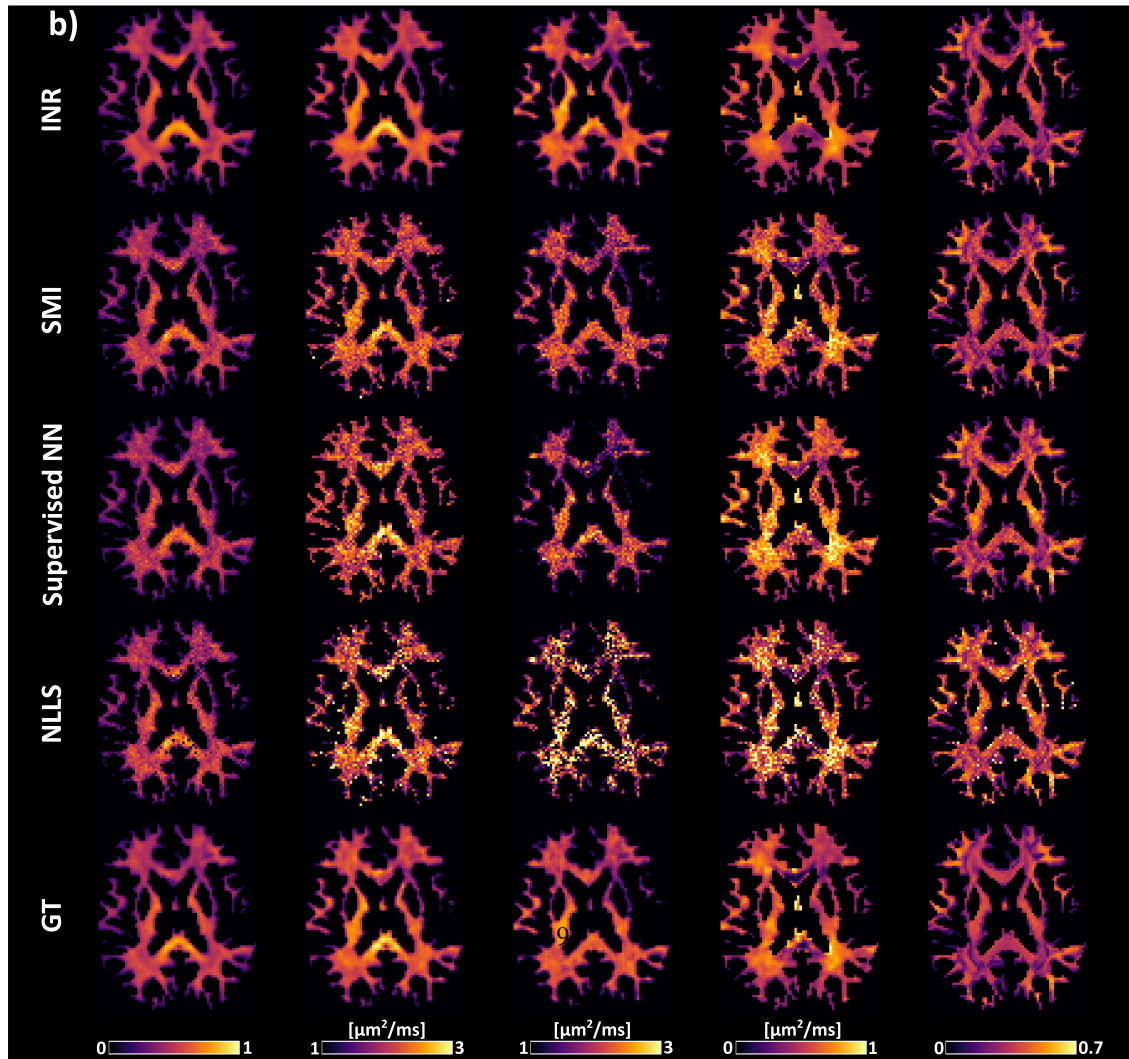
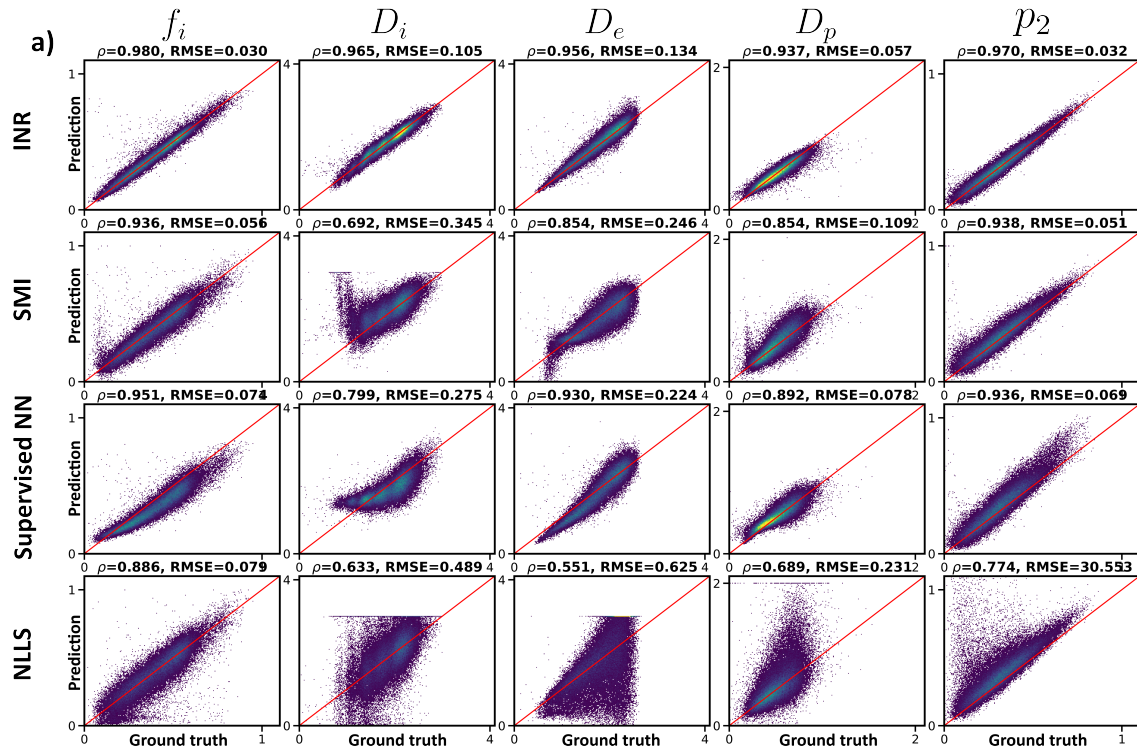


Figure 3: Experiment 1 (SNR 20): **a)** Scatter density plots of ground truth versus parameter estimations of all methods. The titles of the subplots indicate ρ and RMSE. **b)** SM parameter maps corresponding to the results in **a)**. Bottom row shows the ground truth (GT).

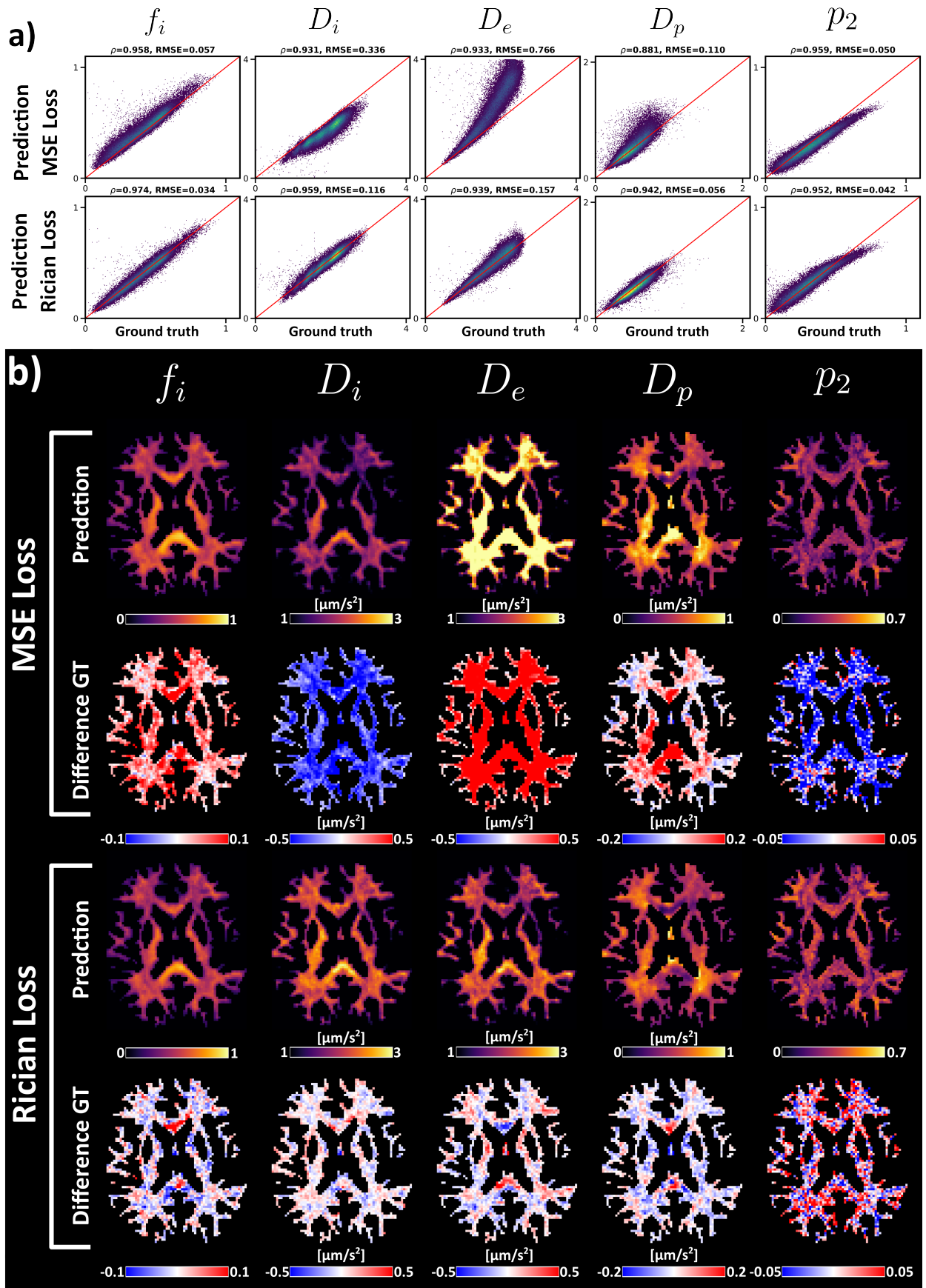


Figure 4: Effect of Rician Loss Likelihood function (SNR = 20). **a)** Scatter plots for estimation with MSE and Rician loss. **b)** Brain parameter maps of the predictions from **a)**. Difference maps are with the ground truth parameters.

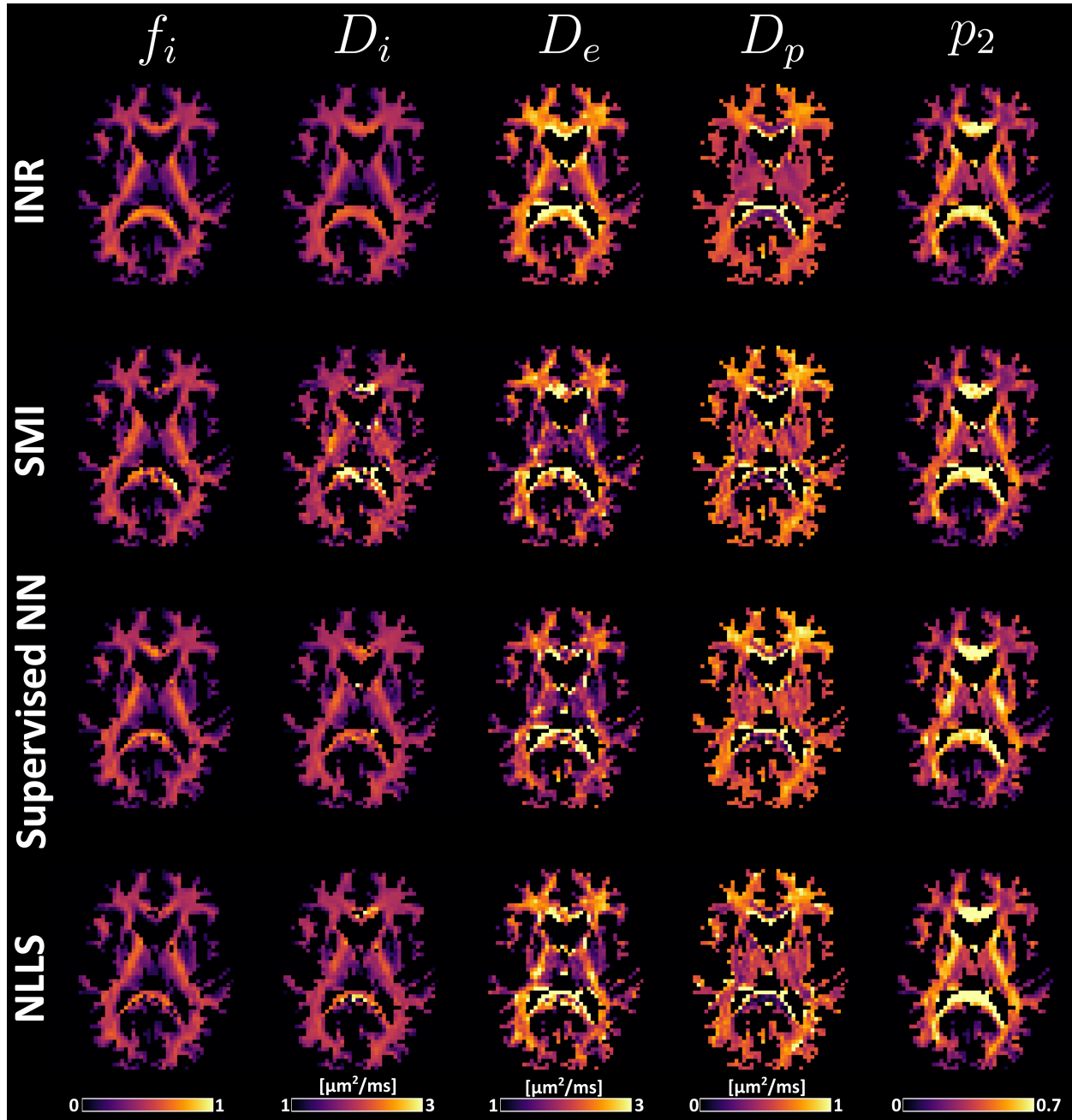


Figure 5: SM parameter maps fitted on in vivo data where each row corresponds to a different method.

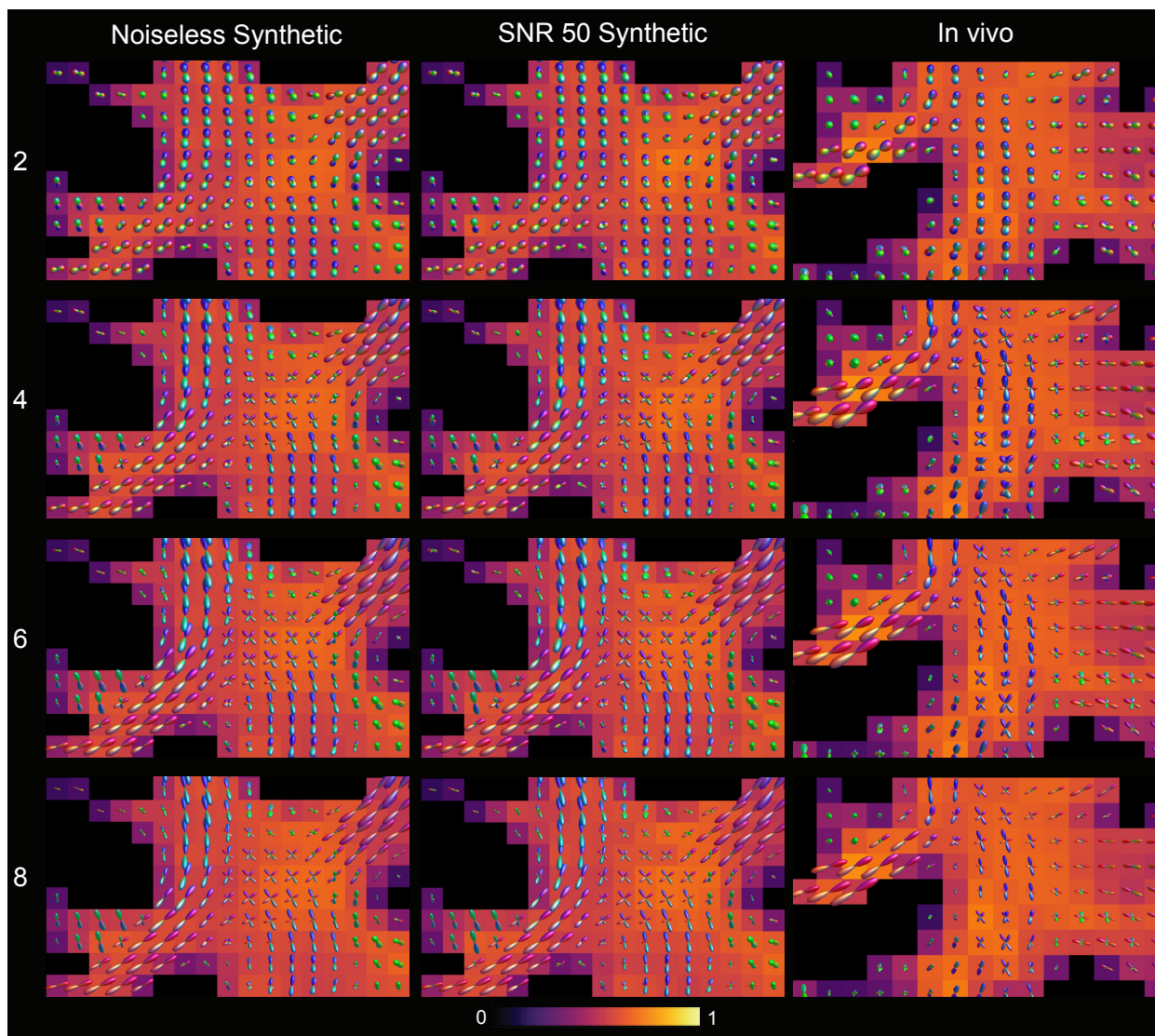


Figure 6: Visualization of the centrum semi-ovale for different SH orders l_{max} (rows) and datasets (columns), with a parameter map of f_i as background. FODs are scaled for visibility.

3.5. Effect of gradient non-uniformity correction of SM parameter estimation

Brain parameter maps with and without gradient non-uniformity correction on in vivo data are presented in Fig. 7. Difference maps show a significant effect on D_i , D_e . Corrected maps show effect at the edges of the brain, mainly in the frontal lobe. This is to be expected as gradient non-uniformity is strongest there. D_i and D_e show lower values after correction. The influence of the correction is least apparent on f_i and p_2 . Training with Rician loss shows the most effect on p_2 estimates.

3.6. Implicit neural representation for spatial interpolation

The visualizations in Figure 8 show the comparison between the p_2 parameter maps using different methods for upsampling. The linear interpolation maintains the pixelated appearance of the low-resolution data, especially visible in structures that are not aligned with the image grid (a 'staircase-like' effect). These artifacts are, although less prominent, still visible in cubic interpolation. The INR does not show these artifacts at this resolution, as the underlying continuous representation is less limited by the input resolution.

3.7. Model fitting times

Model fitting times for all INR experiments are shown in Table 3. The main influence on the fitting time is the size of the dataset (number of voxels in the WM mask), the size of the hidden layers, amount of epochs, the number of outputs (determined by l_{max}) and the usage of the analytical or numerical integration solution. The analytical approach was used in the experiments with the simulated dataset and the numerical approach for the in vivo data. Number of white matter voxels included in the simulated data and in vivo data are 60800 and 11266, respectively. This means that the analytical approach is considerably faster than the numerical approach. Addition of gradient non-uniformity correction also increases fitting time.

l_{max}	2	4	6	8
Synthetic clean (A)	313	448	667	1097
Synthetic SNR 50 Gaussian (A)	320	462	674	1100
Synthetic SNR 50 Rician (MSE, A)	313	-	-	-
Synthetic SNR 50 Rician (Rician loss, A)	321	-	-	-
In vivo (N)	390	563	889	1411
In vivo (Rician loss, N)	391	-	-	-
Gradient non-uniformity correction (N)	516	-	-	-

Table 3: Table showing fitting times in seconds for the INR on different datasets, N = numerical integration, A = analytical integration.

4. Discussion

4.1. Implications of the results

In this work, we show how INRs can be used to estimate continuous, noise-robust SM parameter maps of simulated and in vivo datasets and with different SH orders. The quantitative experiments on synthetic data show how the proposed method outperforms existing methods on noisy data. For high SNR levels (see Fig. B.11), the supervised NN method achieves performance metrics close to those of the INR approach; however, it can be significantly more time-consuming due to its reliance on NLLS for generating part of the training data and the need to retrain the model for each specific acquisition protocol. At higher noise levels (SNR = 20), the INR method clearly outperforms all other methods (see Fig. 3). On in vivo data the underlying representation shows a more structurally correlated appearance, without large inter-voxel variability. This is further illustrated by upsampling the INR at high resolution. Parameter estimates for FOD up to SH order eight can be provided alongside the other SM parameters without introducing bias in other parameters as shown in Appendix D. The unsupervised nature of the method avoids training-set bias prevalent in supervised fitting methods.

The proposed hyperparameters $n_p = 5000$ and $n_h = 2048$ provide a robust setting that can provide good representations of dMRI datasets with different sizes, acquisition protocols, and levels of noise. An exploration of these

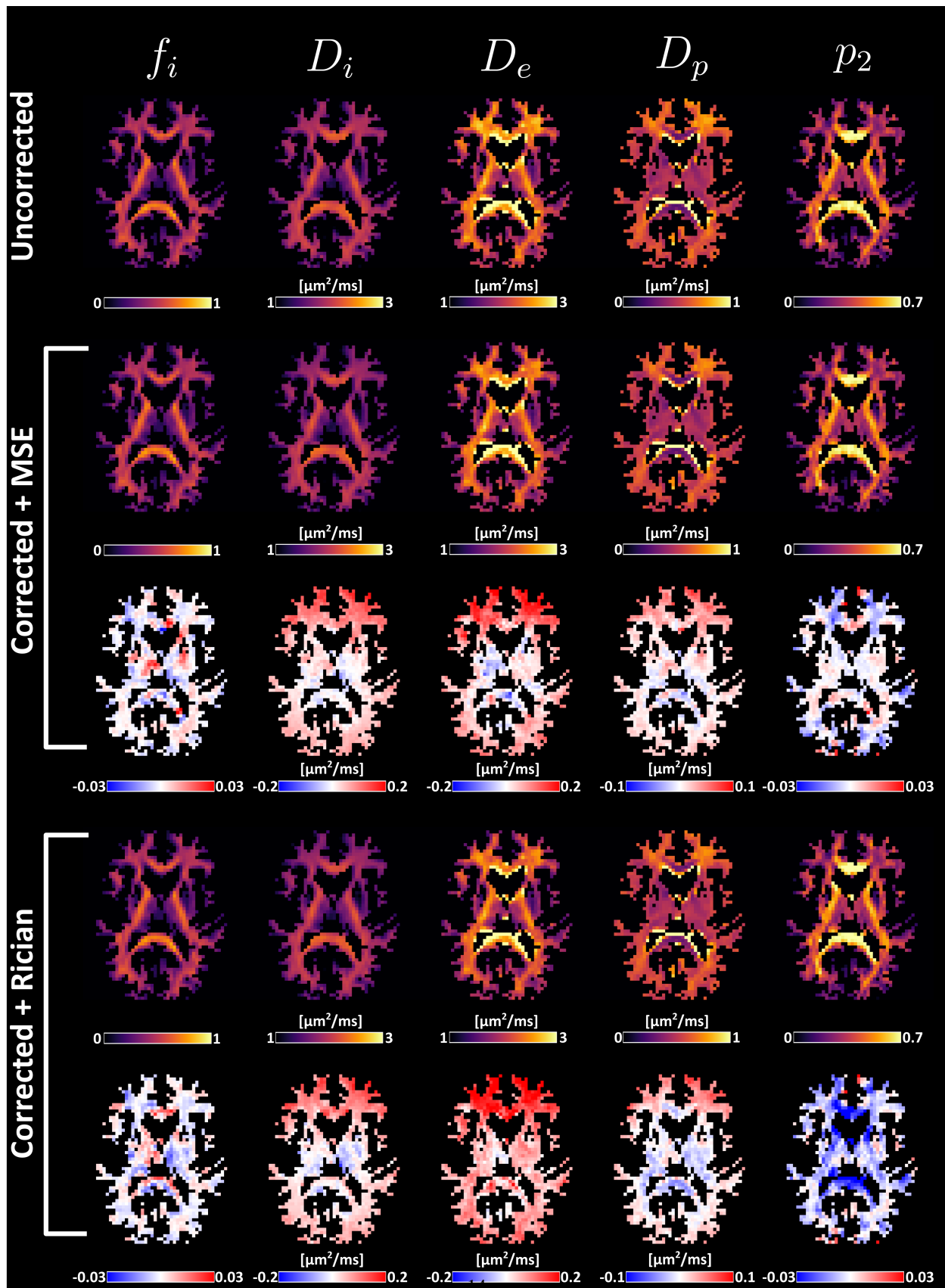


Figure 7: Effect of gradient non-uniformity correction on the estimation of SM parameters. Top row shows parameter maps without correction. Bottom rows show the effect of gradient non-uniformity correction with MSE loss and Rician loss. Difference maps are with respect to prediction with MSE and without gradient non-uniformity correction (top row).

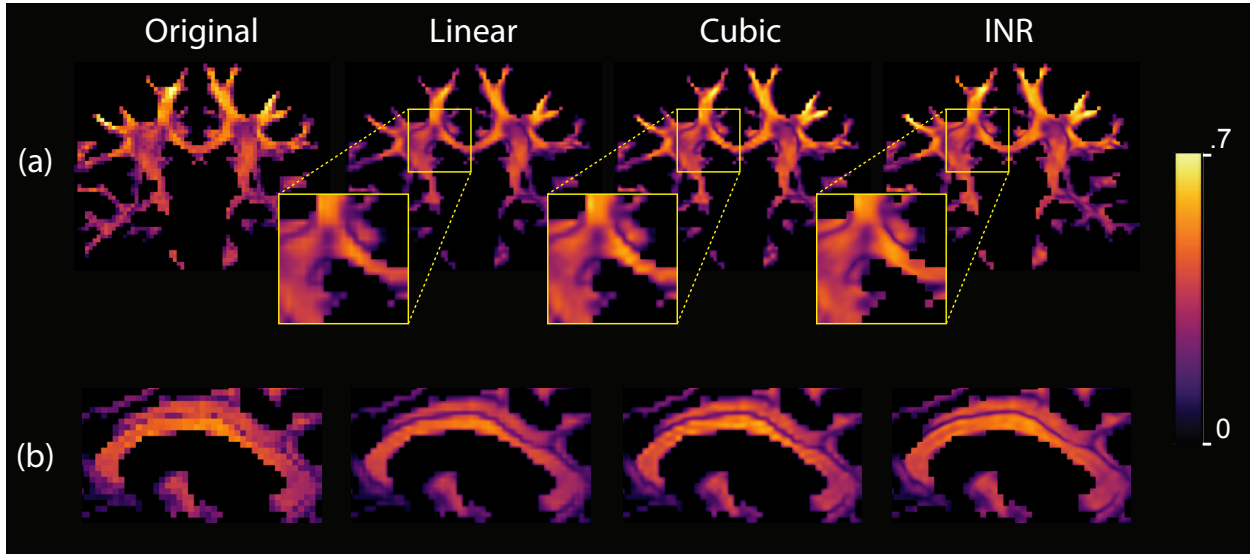


Figure 8: A coronal slice (a) and a sagittal slice (b) of the p_2 parameter map shown at the original resolution, and upsampled 8x in every dimension using linear interpolation, cubic interpolation, and the INR.

hyperparameters can be found in the supplement of (Hendriks et al., 2025). The hyperparameter σ^2 provides a convenient way of tuning the model to provide stronger or weaker spatial regularization, as detailed in Appendix A. Fitting time is a critical factor when applying dMRI microstructure modeling, and various efforts have been made to speed up the computationally heavy nonlinear optimization and enable large-scale population studies (Daducci et al., 2015a; Harms et al., 2017; Diao and Jelescu, 2023). INRs circumvent this through its inherent unsupervised MLP structure, which allows for efficient, continuous representation of the parameter space without requiring voxel-wise optimization. The INRs are fit on consumer grade hardware in around 6 up to at most 23 minutes for the scenarios tested, much faster than classic NLLS approaches. Using the analytical integration approach decreases training time considerably, possible when excluding negative b_Δ values in acquisition protocols. Once the INR is fit to the dataset, the inference time is negligible. For example, an $l_{max} = 2$ model with $n_h = 2048$ and $n_p = 5000$ can perform inference at one million coordinates in 2.7 seconds, including data writing times to and from the GPU. However, since INRs require a model to be fit to every individual dataset, supervised inference remains faster for datasets consisting of many acquisition parameter settings, despite the considerable amount of training time it requires, e.g. for the supervised NN method. Nonetheless, the duration of the fitting process for unsupervised learning in combination with dMRI models have been reduced to seconds when applying transfer learning (Li et al., 2024), which could make on-the-fly fitting of INRs for datasets with a high number of acquisitions possible.

The method’s ability to incorporate gradient non-uniformity correction in the fitting process provides an advantage over typical supervised methods, for which the training set would be impractically large to capture the spatial variability. This correction is essential as even small non-uniformities can affect parameter maps (Bammer et al., 2003; Mesri et al., 2020; Mohammadi et al., 2012; Morez et al., 2021), and the availability of high-performance gradient coils suffering from significant gradient non-uniformities is increasing (Jones et al., 2018). To our knowledge, only method 2 has implemented gradient non-uniformity correction in the SM fitting process (Coelho et al., 2023) using SVD and linear regression methods, which approximates the exact acquisition setting in every voxel.

4.2. Limitations of the approach

The ground truth generated for the synthetic experiments makes use of SMI for generating the underlying parameter maps. This could potentially bias the parameters to be in a range that favors estimation using SMI. We indeed observed that estimation on the noiseless signal showed optimal performance for SMI and NLLS (see Fig. B.10a). Nevertheless, we have attempted to reduce biases towards the estimation for creating the ground truth by smoothing

the parameter maps and using FODs from a different source (MSMT-CSD). Similarly, we used the diffusion parameter distributions found using NLLS on the target dataset to fit the supervised NN to generate the best-case scenario for the distribution of the training dataset. Commonly the supervised NN would depend on parameter distributions from a predefined fixed dataset, because refitting the network for every dataset is prohibitively time-consuming. Another limitation related to the ground truth is that the MGH dataset used in this study contained only linear tensor encoding (LTE), which may have led to inaccurate parameter estimates (see discussion at the end of this section).

The comparison experiments across methods were conducted using Gaussian noise, which differs from the noise characteristics of in vivo magnitude MRI data, typically following Rician or non-central Chi distributions. However, with appropriate preprocessing and ideally the availability of phase data, the noise can be transformed to approximate a Gaussian distribution (Eichner et al., 2015; Koay et al., 2009). This makes the use of Gaussian noise still relevant and consistent with previous work in self-supervised learning for dMRI (Álvaro Planchuelo-Gómez et al., 2024). The Rician noise experiments reveal biases in the parameter estimates by the INR when using MSE, suggesting that this should be taken into consideration. In this work we show the promise of correcting for this bias by using a loss function tailored specifically to Rician noise (Parker et al., 2023).

The interpretation of the in vivo parameter maps is subjective, as there is no ground truth available. The INR produces more spatially coherent estimates than other methods, showing anatomically plausible structure and physiologically plausible parameter values. This could imply that they more closely resemble the actual underlying tissue, but conclusions should be drawn with caution. For example, compared to the other maps the INR produces a slightly higher estimate for D_e and a slightly lower estimate for D_p . We cannot be certain about which estimate is more accurate.

Additionally, correcting for gradient non-uniformities has a significant impact on the parameter estimates, yet the accuracy remains to be evaluated. Both experiments in section 3.2 and 3.5 show that these corrections result in lower estimates for D_e which brings D_e more in agreement with previous work showing $D_i > D_e$ (in gadolinium based contrast experiments (Kunz et al., 2018)) and $D_i \sim 2.3 \mu\text{m}^2/\text{ms}$ (in experiments with elaborate acquisition protocols using high diffusion planar tensor encoding (Dhital et al., 2019)). Any further inconsistency with values of D_e for the in vivo dataset could be caused by the inability of the acquisition protocol to discriminate solution branches as a high b-shell ($b > 5000 \text{ s/mm}^2$) with LTE is lacking (Jelescu et al., 2016; Coelho et al., 2019, 2022). To gain more insight into the degeneracies of the INRs estimation and to enable error quantification, calculating the posterior distribution is required (Consagra et al., 2025; Jallais and Palombo, 2024).

4.3. Future work

The presented INR method can be extended in future work. This work has focused on including the minimal number of SM parameters to reduce the complexity of the fitting parameter space and to evaluate the method’s performance. Importantly, the framework is fully flexible to fit any biophysical model, by adjusting the forward equation to predict the signal (Fig. 2). For example, the SM implementation can be extended to include relaxation effects, which introduce compartmental T_2 as fitting parameters. Further distinction can be made between intra-axonal compartmental T_2 and extra-axonal compartmental T_2 (Tax et al., 2021; Veraart et al., 2018), which adds two extra fitting parameters. The contribution of free water can also be introduced as a fitting parameter. However, previous work has shown that the impact of this parameter is small except for voxels around the ventricles (Coelho et al., 2022). Adding this parameter could resolve fitting issues around the ventricles for the in vivo data in section 3.3 where high D_e and D_p values are found.

The spatial regularization inherent to INRs in the fitting process can be beneficial for other biophysical models. The presented method focuses on white matter and therefore a white matter segmentation was performed. When sampling outside of the white matter (as shown around the edges in Figure 8), the INR produces inaccurate results. Implementation of gray matter models (Palombo et al., 2020) using INRs avoids the need for fitting solely white matter and can provide whole brain parameter maps.

The combination of estimating SM parameters together with FOD SH up to high l_{max} values opens up the possibility to combine the microstructural information of SM-estimates and the directional information of the FOD to do microstructure-informed tractography (Reisert et al., 2014; Daducci et al., 2015b; Girard et al., 2017; Consagra et al., 2025), and future work could extend the model to estimate fiber-direction specific kernels. Tractography can also benefit from the continuous representation of the INR in both interpolation computation time and accuracy (Spears and Fletcher, 2024).

The application of microstructural information in clinical studies remains untested in this context, but its potential

utility for the diagnosis and assessment of various pathophysiological processes could be explored. The INRs performance remains to be further evaluated in pathology, particularly the effect of spatial regularization on the quantification of small lesions. The encoding frequency variance σ can be tuned to accommodate higher frequency changes in the signal.

4.4. Conclusion

Using INRs to fit the SM provides noise-robust, spatially regularized parameter estimates. FODs of SH orders up to at least eight can be estimated alongside the SM kernel parameters. The unsupervised nature of this approach has advantages over existing (supervised) methods, as it prevents training set bias and allows for explicit correction of gradient non-uniformities, within reasonable estimation times.

5. Data availability

The MGH Connectome Diffusion Microstructure Dataset (Tian et al., 2022b) is publicly available. The synthetic and in-vivo dataset can be made available upon reasonable request.

6. Code availability

The code used to generate the results in this paper is publicly available through github at: https://github.com/tomhend/Standard_model_INR.

7. Acknowledgements

We thank Dennis Klomp for input to the manuscript. CMWT is supported by a Vidi grant (21299) from the Dutch Research Council (NWO) and a Sir Henry Wellcome Fellowship (215944/Z/19/Z). Data were provided [in part] by the Human Connectome Project, MGH-USC Consortium (Principal Investigators: Bruce R. Rosen, Arthur W. Toga and Van Wedeen; U01MH093765) funded by the NIH Blueprint Initiative for Neuroscience Research grant; the National Institutes of Health grant P41EB015896; and the Instrumentation Grants S10RR023043, 1S10RR023401, 1S10RR019307.

References

- Alexander, D.C., Dyrby, T.B., Nilsson, M., Zhang, H., 2019. Imaging brain microstructure with diffusion MRI: practicality and applications. *NMR in Biomedicine* 32, 1–26. doi:10.1002/nbm.3841.
- de Almeida Martins, J.P., Nilsson, M., Lampinen, B., Palombo, M., While, P.T., Westin, C.F., Szczepankiewicz, F., 2021. Neural networks for parameter estimation in microstructural MRI: Application to a diffusion-relaxation model of white matter. *NeuroImage* 244. doi:10.1016/j.neuroimage.2021.118601.
- Alotaibi, A., Podlasek, A., AlTokhis, A., Aldhebaib, A., Dineen, R.A., Constantinescu, C.S., 2021. Investigating microstructural changes in white matter in multiple sclerosis: A systematic review and meta-analysis of neurite orientation dispersion and density imaging. *Brain Sciences* 11, 1151. doi:10.3390/brainsci11091151.
- Bammer, R., Markl, M., Barnett, A., Acar, B., Alley, M.T., Pelc, N.J., Glover, G.H., Moseley, M.E., 2003. Analysis and generalized correction of the effect of spatial gradient field distortions in diffusion-weighted imaging. *Magnetic Resonance in Medicine* 50, 560–569. doi:10.1002/mrm.10545.
- Basser, P.J., Mattiello, J., LeBihan, D., 1994. Mr diffusion tensor spectroscopy and imaging. *Biophysical journal* 66, 259–267. URL: [https://doi.org/10.1016/S0006-3495\(94\)80775-1](https://doi.org/10.1016/S0006-3495(94)80775-1), doi:10.1016/S0006-3495(94)80775-1.
- Coelho, S., Baete, S.H., Lemberskiy, G., Ades-Aron, B., Barrol, G., Veraart, J., Novikov, D.S., Fieremans, E., 2022. Reproducibility of the Standard Model of diffusion in white matter on clinical MRI systems. *NeuroImage* 257. doi:10.1016/j.neuroimage.2022.119290.
- Coelho, S., Lemberskiy, G., Zhu, A., Abad, N., Foo, T.K.F., Fieremans, E., Novikov, D.S., 2023. What if every voxel was measured with a different diffusion protocol?, in: *Proceedings of the ISMRM 2023, International Society for Magnetic Resonance in Medicine, Toronto, Canada*. Presented at the Annual Meeting of the ISMRM.
- Coelho, S., Pozo, J.M., Jespersen, S.N., Jones, D.K., Frangi, A.F., 2019. Resolving degeneracy in diffusion mri biophysical model parameter estimation using double diffusion encoding. *Magnetic Resonance in Medicine* 82, 395–410. URL: <https://onlinelibrary.wiley.com/doi/abs/10.1002/mrm.27714>, doi:<https://doi.org/10.1002/mrm.27714>, arXiv:<https://onlinelibrary.wiley.com/doi/pdf/10.1002/mrm.27714>.

- Consagra, W., Ning, L., Rathi, Y., 2024. Neural orientation distribution fields for estimation and uncertainty quantification in diffusion mri. *Medical Image Analysis* 93, 103105.
- Consagra, W., Ning, L., Rathi, Y., 2025. A deep learning approach to multi-fiber parameter estimation and uncertainty quantification in diffusion mri. *Medical Image Analysis*, 103537.
- Daducci, A., Canales-Rodríguez, E.J., Zhang, H., Dyrby, T.B., Alexander, D.C., Thiran, J.P., 2015a. Accelerated microstructure imaging via convex optimization (amico) from diffusion mri data. *NeuroImage* 105, 32–44. URL: <https://www.sciencedirect.com/science/article/pii/S1053811914008519>, doi:<https://doi.org/10.1016/j.neuroimage.2014.10.026>.
- Daducci, A., Dal Palù, A., Lemkaddem, A., Thiran, J.P., 2015b. Commit: Convex optimization modeling for microstructure informed tractography. *IEEE Transactions on Medical Imaging* 34, 246–257. doi:10.1109/TMI.2014.2352414.
- Dhital, B., Reisert, M., Kellner, E., Kiselev, V.G., 2019. Intra-axonal diffusivity in brain white matter. *NeuroImage* 189, 543–550. URL: <https://www.sciencedirect.com/science/article/pii/S1053811919300151>, doi:<https://doi.org/10.1016/j.neuroimage.2019.01.015>.
- Diao, Y., Jelescu, I., 2023. Parameter estimation for wmti-watson model of white matter using encoder–decoder recurrent neural network. *Magnetic Resonance in Medicine* 89, 1193–1206. URL: <https://onlinelibrary.wiley.com/doi/abs/10.1002/mrm.29495>, doi:<https://doi.org/10.1002/mrm.29495>, arXiv:<https://onlinelibrary.wiley.com/doi/pdf/10.1002/mrm.29495>.
- Dugas, C., Bengio, Y., Bélisle, F., Nadeau, C., Garcia, R., 2000. Incorporating second-order functional knowledge for better option pricing. *Advances in neural information processing systems* 13.
- Eichner, C., Cauley, S.F., Cohen-Adad, J., Möller, H.E., Turner, R., Setsompop, K., Wald, L.L., 2015. Real diffusion-weighted mri enabling true signal averaging and increased diffusion contrast. *NeuroImage* 122, 373–384. URL: <https://www.sciencedirect.com/science/article/pii/S1053811915006941>, doi:<https://doi.org/10.1016/j.neuroimage.2015.07.074>.
- Fieremans, E., Jensen, J.H., Helpert, J.A., 2011. White matter characterization with diffusional kurtosis imaging. *NeuroImage* 58, 177–188. URL: <https://www.sciencedirect.com/science/article/pii/S1053811911006148>, doi:<https://doi.org/10.1016/j.neuroimage.2011.06.006>.
- Fischl, B., 2012. Freesurfer. *NeuroImage* 62, 774–781. doi:<https://doi.org/10.1016/j.neuroimage.2012.01.021>.
- Garyfallidis, E., Brett, M., Amirkhikian, B., Rokem, A., Van Der Walt, S., Descoteaux, M., Nimmo-Smith, I., et al., 2014. Dipy, a library for the analysis of diffusion mri data. *Frontiers in Neuroinformatics* 8, 8. URL: <https://doi.org/10.3389/fninf.2014.00008>, doi:10.3389/fninf.2014.00008.
- Girard, G., Daducci, A., Petit, L., Thiran, J.P., Whittingstall, K., Deriche, R., Wassermann, D., Descoteaux, M., 2017. Ax tract: Toward microstructure informed tractography. *Human brain mapping* 38, 5485–5500.
- Gyori, N.G., Palombo, M., Clark, C.A., Zhang, H., Alexander, D.C., 2022. Training data distribution significantly impacts the estimation of tissue microstructure with machine learning. *Magnetic Resonance in Medicine* 87, 932–947. doi:10.1002/mrm.29014.
- Gómez, P., Toftevaag, H.H., Meoni, G., 2021. torchquad: Numerical integration in arbitrary dimensions with pytorch. *Journal of Open Source Software* 6, 3439. URL: <https://doi.org/10.21105/joss.03439>, doi:10.21105/joss.03439.
- Harms, R., Fritz, F., Tobisch, A., Goebel, R., Roebroeck, A., 2017. Robust and fast nonlinear optimization of diffusion mri microstructure models. *NeuroImage* 155, 82–96. URL: <https://www.sciencedirect.com/science/article/pii/S1053811917303178>, doi:<https://doi.org/10.1016/j.neuroimage.2017.04.064>.
- Hendriks, T., Vilanova, A., Chamberland, M., 2023. Neural spherical harmonics for structurally coherent continuous representation of diffusion mri signal, in: *International Workshop on Computational Diffusion MRI*, Springer. pp. 1–12.
- Hendriks, T., Vilanova, A., Chamberland, M., 2025. Implicit neural representation of multi-shell constrained spherical deconvolution for continuous modeling of diffusion mri. *Imaging Neuroscience* 3, imag.a.00501.
- Henriques, R.N., Tax, C.M.W., Shemesh, N., Veraart, J., 2025. Biophysical modeling of the white matter: from theory towards clinical practice, in: *Meeting Abstract #1008*, [Conference or Organization Name], Champalimaud Research, Champalimaud Centre for the Unknown, Lisbon, Portugal.
- Jallais, M., Palombo, M., 2024. Introducing μ guide for quantitative imaging via generalized uncertainty-driven inference using deep learning. *eLife* 13, RP101069. URL: <https://doi.org/10.7554/eLife.101069>, doi:10.7554/eLife.101069.
- Jelescu, I.O., Palombo, M., Bagnato, F., Schilling, K.G., 2020. Challenges for biophysical modeling of microstructure. *Journal of Neuroscience Methods* 344, 108861. URL: <https://www.sciencedirect.com/science/article/pii/S0165027020302843>, doi:<https://doi.org/10.1016/j.jneumeth.2020.108861>.
- Jelescu, I.O., Veraart, J., Fieremans, E., Novikov, D.S., 2016. Degeneracy in model parameter estimation for multi-compartmental diffusion in neuronal tissue. *NMR in Biomedicine* 29, 33–47. URL: <https://analyticalsciencejournals.onlinelibrary.wiley.com/doi/abs/10.1002/nbm.3450>, doi:<https://doi.org/10.1002/nbm.3450>.
- Jespersen, S.N., Kroenke, C.D., Østergaard, L., Ackerman, J.J., Yablonskiy, D.A., 2007. Modeling dendrite density from magnetic resonance diffusion measurements. *NeuroImage* 34, 1473–1486. doi:10.1016/j.neuroimage.2006.10.037.
- Jeurissen, B., Tournier, J.D., Dhollander, T., Connelly, A., Sijbers, J., 2014. Multi-tissue constrained spherical deconvolution for improved analysis of multi-shell diffusion mri data. *NeuroImage* 103, 411–426.
- Jones, D.K., Alexander, D.C., Bowtell, R., Cercignani, M., Dell'Acqua, F., McHugh, D.J., Miller, K.L., Palombo, M., Parker, G.J., Rudrapatna, U.S., Tax, C.M., 2018. Microstructural imaging of the human brain with a 'super-scanner': 10 key advantages of ultra-strong gradients for diffusion MRI. doi:10.1016/j.neuroimage.2018.05.047.
- Kaden, E., Kelm, N.D., Carson, R.P., Does, M.D., Alexander, D.C., 2016. Multi-compartment microscopic diffusion imaging. *NeuroImage* 139, 346–359. URL: <https://www.sciencedirect.com/science/article/pii/S1053811916302063>, doi:<https://doi.org/10.1016/j.neuroimage.2016.06.002>.
- Kim, D.H., Laun, D.H., Kamesh, N.B., et al., 2016. Diffusion microstructure imaging of the substantia nigra in parkinson's disease using mean apparent propagator mri. *NeuroImage Clin* 12, 451–459. doi:10.1016/j.nicl.2016.08.006.
- Koay, C.G., Özarslan, E., Pierpaoli, C., 2009. Probabilistic identification and estimation of noise (piesno): A self-consistent approach and its applications in mri. *Journal of Magnetic Resonance* 199, 94–103. URL: <https://www.sciencedirect.com/science/article/pii/>

- S1090780709000767, doi:<https://doi.org/10.1016/j.jmr.2009.03.005>.
- Kroenke, C.D., Ackerman, J.J., Yablonskiy, D.A., 2004. On the nature of the naa diffusion attenuated mr signal in the central nervous system. *Magnetic Resonance in Medicine* 52, 1052–1059. URL: <https://onlinelibrary.wiley.com/doi/abs/10.1002/mrm.20260>, doi:<https://doi.org/10.1002/mrm.20260>, arXiv:<https://onlinelibrary.wiley.com/doi/pdf/10.1002/mrm.20260>.
- Kunz, N., da Silva, A.R., Jelescu, I.O., 2018. Intra- and extra-axonal axial diffusivities in the white matter: Which one is faster? *NeuroImage* 181, 314–322. URL: <https://www.sciencedirect.com/science/article/pii/S1053811918306359>, doi:<https://doi.org/10.1016/j.neuroimage.2018.07.020>.
- Lampinen, B., Szczepankiewicz, F., Lätt, J., Knutsson, L., Mårtensson, J., Björkman-Burtscher, I.M., van Westen, D., Sundgren, P.C., Ståhlberg, F., Nilsson, M., 2023. Probing brain tissue microstructure with mri: principles, challenges, and the role of multidimensional diffusion-relaxation encoding. *NeuroImage* 282, 120338. URL: <https://www.sciencedirect.com/science/article/pii/S1053811923004895>, doi:<https://doi.org/10.1016/j.neuroimage.2023.120338>.
- Lampinen, B., Szczepankiewicz, F., Mårtensson, J., van Westen, D., Hansson, O., Westin, C.F., Nilsson, M., 2020. Towards unconstrained compartment modeling in white matter using diffusion-relaxation MRI with tensor-valued diffusion encoding. *Magnetic Resonance in Medicine* 84, 1605–1623. doi:10.1002/mrm.28216.
- Li, Z., Li, Z., Bilgic, B., Lee, H.H., Ying, K., Huang, S.Y., Liao, H., Tian, Q., 2024. DIMOND: Diffusion Model Optimization with Deep Learning. *Advanced Science* doi:10.1002/advs.202307965.
- Liao, Y., Coelho, S., Chen, J., Ades-Aron, B., Pang, M., Stepanov, V., Osorio, R., Shepherd, T., Lui, Y.W., Novikov, D.S., Fieremans, E., 2024. Mapping tissue microstructure of brain white matter in vivo in health and disease using diffusion MRI. *Imaging Neuroscience* 2, 1–17. doi:10.1162/imagf\{}_a\{}_00102.
- Mesri, H.Y., David, S., Viergever, M.A., Leemans, A., 2020. The adverse effect of gradient nonlinearities on diffusion mri: From voxels to group studies. *NeuroImage* 205, 116127. URL: <https://www.sciencedirect.com/science/article/pii/S1053811919307189>, doi:<https://doi.org/10.1016/j.neuroimage.2019.116127>.
- Mohammadi, S., Nagy, Z., Möller, H.E., Symms, M.R., Carmichael, D.W., Josephs, O., Weiskopf, N., 2012. The effect of local perturbation fields on human dti: Characterisation, measurement and correction. *NeuroImage* 60, 562–570. URL: <https://www.sciencedirect.com/science/article/pii/S105381191101411X>, doi:<https://doi.org/10.1016/j.neuroimage.2011.12.009>.
- Morez, J., Sijbers, J., Vanhevel, F., Jeurissen, B., 2021. Constrained spherical deconvolution of nonspherically sampled diffusion mri data. *Human Brain Mapping* 42, 521–538. URL: <https://onlinelibrary.wiley.com/doi/abs/10.1002/hbm.25241>, doi:<https://doi.org/10.1002/hbm.25241>, arXiv:<https://onlinelibrary.wiley.com/doi/pdf/10.1002/hbm.25241>.
- Novikov, D.S., Fieremans, E., Jespersen, S.N., Kiselev, V.G., 2019. Quantifying brain microstructure with diffusion MRI: Theory and parameter estimation. *NMR in Biomedicine* 32, 1–53. doi:10.1002/nbm.3998.
- Novikov, D.S., Veraart, J., Jelescu, I.O., Fieremans, E., 2018. Rotationally-invariant mapping of scalar and orientational metrics of neuronal microstructure with diffusion mri. *NeuroImage* 174, 518–538. URL: <https://www.sciencedirect.com/science/article/pii/S1053811918301915>, doi:<https://doi.org/10.1016/j.neuroimage.2018.03.006>.
- Palombo, M., Ianus, A., Guerri, M., Nunes, D., Alexander, D.C., Shemesh, N., Zhang, H., 2020. Sandi: A compartment-based model for non-invasive apparent soma and neurite imaging by diffusion mri. *NeuroImage* 215, 116835. URL: <https://www.sciencedirect.com/science/article/pii/S1053811920303220>, doi:<https://doi.org/10.1016/j.neuroimage.2020.116835>.
- Parker, C.S., Schroder, A., Epstein, S.C., Cole, J., Alexander, D.C., Zhang, H., 2023. Rician likelihood loss for quantitative mri using self-supervised deep learning. URL: <https://arxiv.org/abs/2307.07072>, arXiv:2307.07072.
- Parker, T.D., Slatery, C.F., Zhang, J., Nicholas, J.M., Paterson, R.W., Foulkes, A.J., Malone, I.B., Thomas, D.L., Modat, M., Cash, D.M., Crutch, S.J., Alexander, D.C., Ourselin, S., Fox, N.C., Zhang, H., Schott, J.M., 2018. Cortical microstructure in young onset alzheimer’s disease using neurite orientation dispersion and density imaging. *Human Brain Mapping* 39, 3005–3017. doi:10.1002/hbm.24056.
- Álvaro Planchuelo-Gómez, Descoteaux, M., Larochelle, H., Hutter, J., Jones, D.K., Tax, C.M., 2024. Optimisation of quantitative brain diffusion-relaxation mri acquisition protocols with physics-informed machine learning. *Medical Image Analysis* 94, 103134. URL: <https://www.sciencedirect.com/science/article/pii/S1361841524000598>, doi:<https://doi.org/10.1016/j.media.2024.103134>.
- Reisert, M., Kellner, E., Dhital, B., Hennig, J., Kiselev, V.G., 2017. Disentangling micro from mesostructure by diffusion MRI: A Bayesian approach. *NeuroImage* 147, 964–975. doi:10.1016/j.neuroimage.2016.09.058.
- Reisert, M., Kiselev, V.G., Dhital, B., Kellner, E., Novikov, D.S., 2014. Mesoft: Unifying diffusion modelling and fiber tracking, in: Golland, P., Hata, N., Barillot, C., Hornegger, J., Howe, R. (Eds.), *Medical Image Computing and Computer-Assisted Intervention – MICCAI 2014*, Springer International Publishing, Cham, pp. 201–208.
- Sjölund, J., Szczepankiewicz, F., Nilsson, M., Topgaard, D., Westin, C.F., Knutsson, H., 2015. Constrained optimization of gradient waveforms for generalized diffusion encoding. *Journal of Magnetic Resonance* 261, 157–168. URL: <https://www.sciencedirect.com/science/article/pii/S1090780715002451>, doi:<https://doi.org/10.1016/j.jmr.2015.10.012>.
- Spears, T., Fletcher, P.T., 2024. Learning spatially-continuous fiber orientation functions, in: *2024 IEEE International Symposium on Biomedical Imaging (ISBI)*, IEEE, pp. 1–5.
- Tancik, M., Srinivasan, P., Mildenhall, B., Fridovich-Keil, S., Raghavan, N., Singhal, U., Ramamoorthi, R., Barron, J., Ng, R., 2020. Fourier features let networks learn high frequency functions in low dimensional domains. *Advances in neural information processing systems* 33, 7537–7547.
- Tax, C.M.W., Kleban, E., Chamberland, M., Barakovi, M., Rudrapatna, U., Jones, D.K., 2021. NeuroImage Measuring compartmental ? 2-orientational dependence in human brain white matter using a tilttable RF coil and diffusion- ? 2 correlation MRI 236. doi:10.1016/j.neuroimage.2021.117967.
- Tian, Q., Fan, Q., Witzel, T., Polackal, M.N., Ohringer, N.A., Ngamsombat, C., et al., 2022a. Comprehensive diffusion mri dataset for in vivo human brain microstructure mapping using 300 mt/m gradients. *figshare*. Collection. URL: <https://doi.org/10.6084/m9.figshare.c.5315474.v1>, doi:10.6084/m9.figshare.c.5315474.v1.
- Tian, Q., Fan, Q., Witzel, T., Polackal, M.N., Ohringer, N.A., Ngamsombat, C., Russo, A.W., Machado, N., Brewer, K., Wang, F., Setsompom, K., Polimeni, J.R., Keil, B., Wald, L.L., Rosen, B.R., Klawiter, E.C., Nummenmaa, A., Huang, S.Y., 2022b. Comprehensive diffusion MRI dataset

- for in vivo human brain microstructure mapping using 300 mT/m gradients. *Scientific Data* 9. doi:10.1038/s41597-021-01092-6.
- Tournier, J.D., Calamante, F., Connelly, A., a. Robust determination of the fibre orientation distribution in diffusion MRI: Non-negativity constrained super-resolved spherical deconvolution 35, 1459–1472. URL: <https://www.sciencedirect.com/science/article/pii/S1053811907001243>.
- Tournier, J.D., Calamante, F., Connelly, A., 2007. Robust determination of the fibre orientation distribution in diffusion MRI: Non-negativity constrained super-resolved spherical deconvolution. *NeuroImage* 35, 1459–1472. doi:10.1016/j.neuroimage.2007.02.016.
- Tournier, J.D., Smith, R., Raffelt, D., Tabbara, R., Dhollander, T., Pietsch, M., Christiaens, D., Jeurissen, B., Yeh, C.H., Connelly, A., b. MRtrix3: A fast, flexible and open software framework for medical image processing and visualisation 202, 116137. doi:10.1016/j.neuroimage.2019.116137, arXiv:31473352.
- Veraart, J., Novikov, D.S., Christiaens, D., Ades-aron, B., Sijbers, J., Fieremans, E., 2016. Denoising of diffusion MRI using random matrix theory. *NeuroImage* 142, 394–406. doi:10.1016/j.neuroimage.2016.08.016.
- Veraart, J., Novikov, D.S., Fieremans, E., 2018. Te dependent diffusion imaging (teddi) distinguishes between compartmental t2 relaxation times. *NeuroImage* 182, 360–369. URL: <https://www.sciencedirect.com/science/article/pii/S1053811917307784>, doi:<https://doi.org/10.1016/j.neuroimage.2017.09.030>. microstructural Imaging.
- Westin, C.F., Szczepankiewicz, F., Pasternak, O., Özarslan, E., Topgaard, D., Knutsson, H., Nilsson, M., 2014. Measurement tensors in diffusion mri: Generalizing the concept of diffusion encoding, in: Golland, P., Hata, N., Barillot, C., Hornegger, J., Howe, R. (Eds.), *Medical Image Computing and Computer-Assisted Intervention – MICCAI 2014*, Springer International Publishing, Cham. pp. 209–216.
- Zhang, H., Schneider, T., Wheeler-Kingshott, C.A., Alexander, D.C., 2012. Noddi: Practical in vivo neurite orientation dispersion and density imaging of the human brain. *NeuroImage* 61, 1000–1016. URL: <https://www.sciencedirect.com/science/article/pii/S1053811912003539>, doi:<https://doi.org/10.1016/j.neuroimage.2012.03.072>.

Appendix A. Choice of hyperparameter σ^2

The Fourier Feature (Tancik et al., 2020) encoding provides an additional hyperparameter σ^2 that controls the width of the normal distribution where the encoding frequencies are sampled from. This provides extra flexibility to the user to control the spatial regularization of the representation. Lower σ^2 yields lower frequencies, which capture less detail and noise, while higher σ^2 does the opposite. This implies that downstream tasks which do not require exceptionally fine details could benefit from lower σ^2 to mitigate noise, while higher quality datasets can be modeled with higher σ^2 to maintain contrast in regions with high frequency changes in signal.

To illustrate the effect σ^2 has on the representation, we fit an INR on the synthetic datasets with Gaussian noise SNR 50 and 20 for each $\sigma^2 \in \{1, 2, 4, 8\}$. The D_i parameter map is visualized for every INR in Figure A.9. At $\sigma^2 = 1$ we

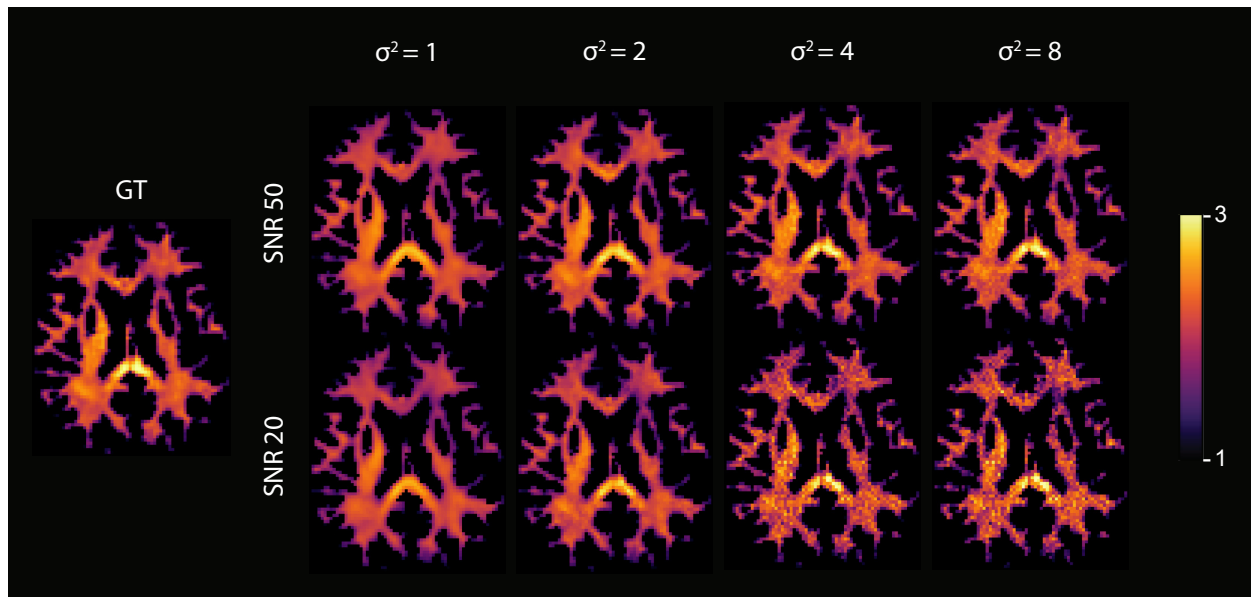


Figure A.9: Parameter maps of D_i for the INR fit on the synthetic datasets with SNR 50 and 20 (rows) with varying σ^2 (columns)

see an overly smooth representation, losing some finer detail. These details start to re-appear at $\sigma^2 = 2$. While for SNR 50 the $\sigma^2 = 4$ still provides a good representation, for SNR 20 the INR starts capturing too much of the noise. For $\sigma^2 = 8$ both datasets produce an overly granular parameter map. In general we would recommend starting with $\sigma^2 = 3.5$, and move up or down based on downstream requirements and dataset quality.

Appendix B. Noise comparison

Scatter density plots from Fig.B.10a demonstrate that the most accurate voxel-wise estimates are obtained with NLLS in the noiseless case as expected, where $\rho > 0.999$. Only RMSE of p_2 deviates notably, which is attributed to the lack of constraints on the fODF coefficient values in the NLLS method, leading to outliers. Method 3 also shows high correlation for the kernel ($\rho > 0.995$) but shows low accuracy for p_2 . Method 1 shows the lowest accuracy for f_i and D_p . Method 2 performs very accurately for the bulk of the voxels, e.g. less broad scatter density plots than Method 1, but shows high RMSE values for D_i and D_e due to outliers at low ground truth diffusivity values. Visual inspection of the brain parameter maps in Fig. B.10b shows that all fitting methods are capable of producing smooth parameter maps, similar to the ground truth.

Fig.B.11 shows results for experiment 1 where Gaussian noise is considered with SNR 20. The INR method shows to be noise robust also at higher noise levels and outperforms the other methods. Note the spatial smoothness of the parameter maps estimated by the INR method compared to the other very noisy maps.

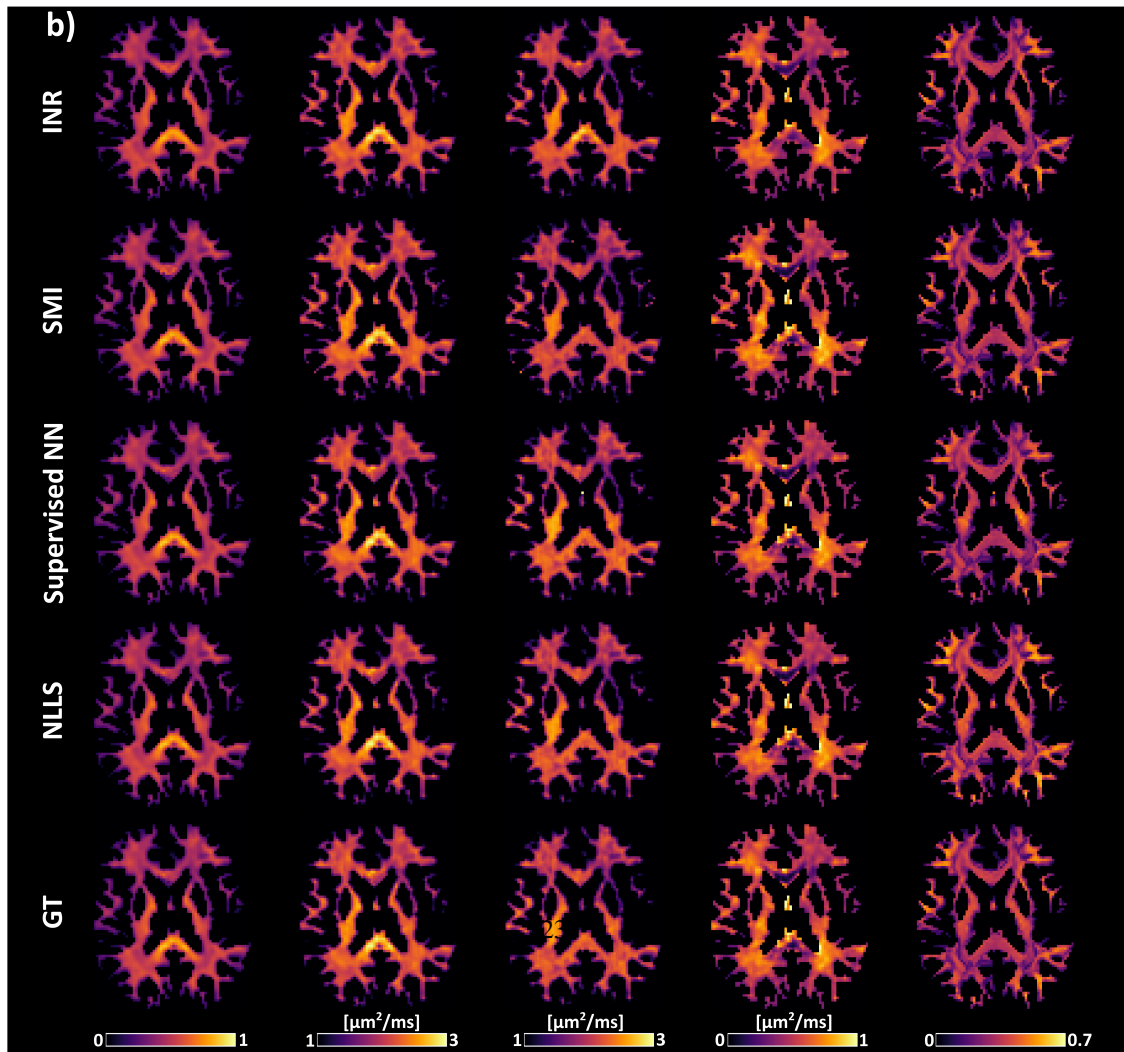
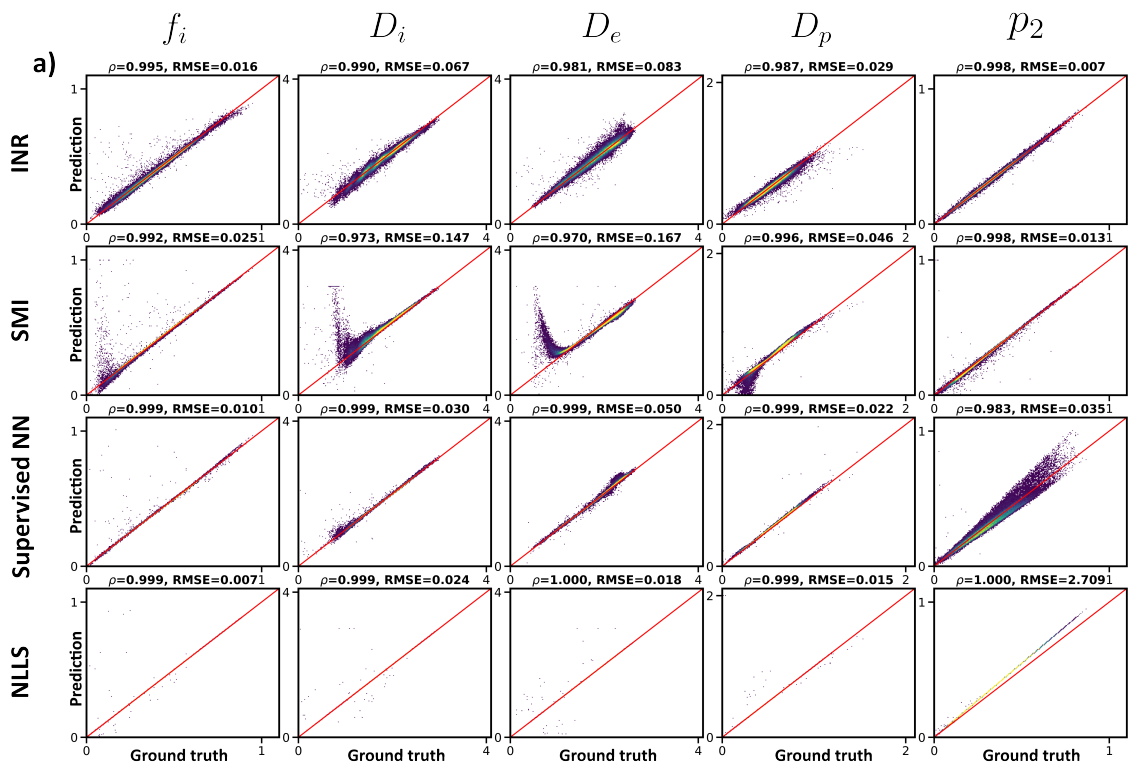


Figure B.10: Experiment 1 (No Noise): **a)** Scatter density plots of the ground truth versus the parameter estimations of all methods. Row numbers correspond to method numbering from section 2.8.1. The titles of the subplots indicate ρ and RMSE. **b)** SM parameter maps corresponding to the results in **a**. Bottom row shows the ground truth (GT).

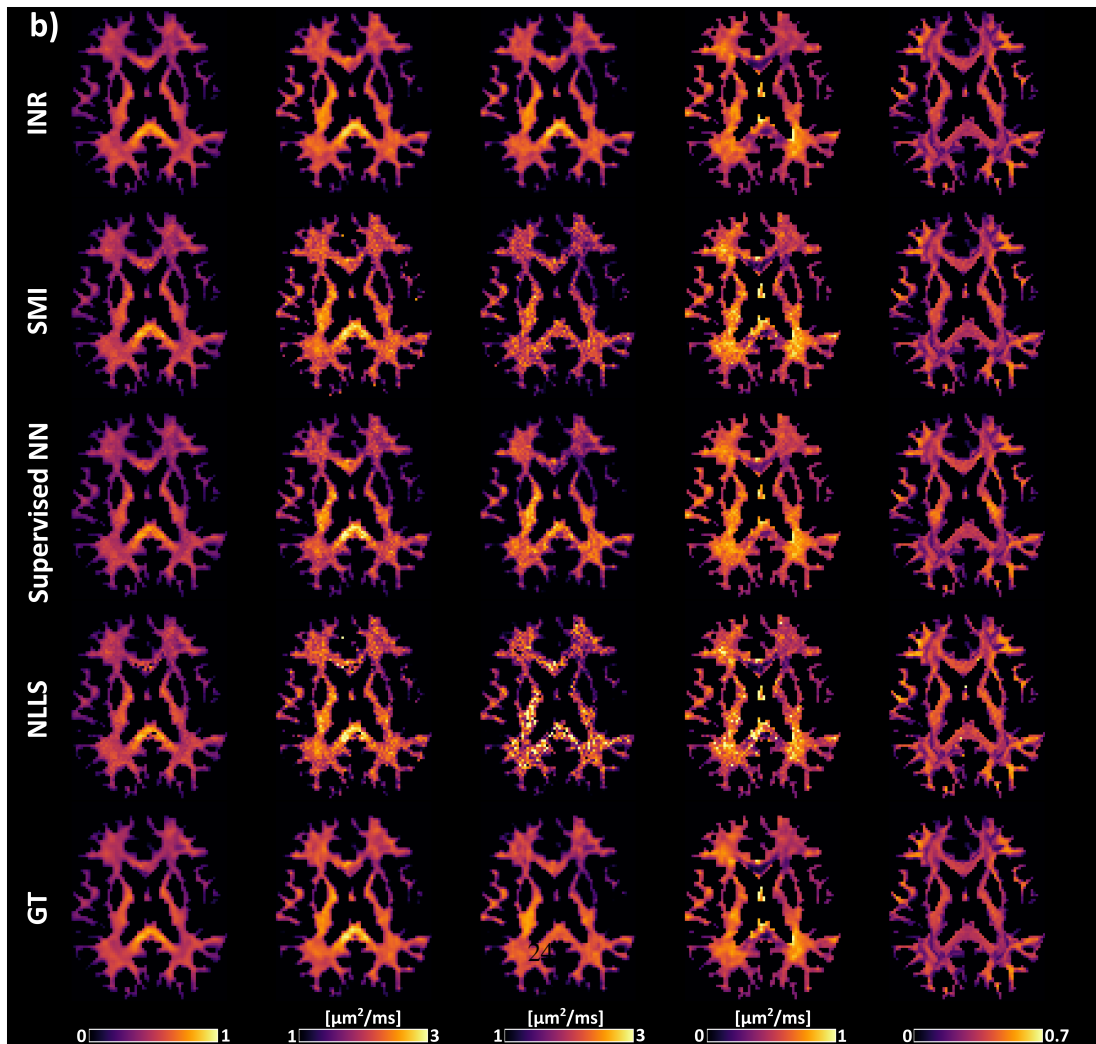
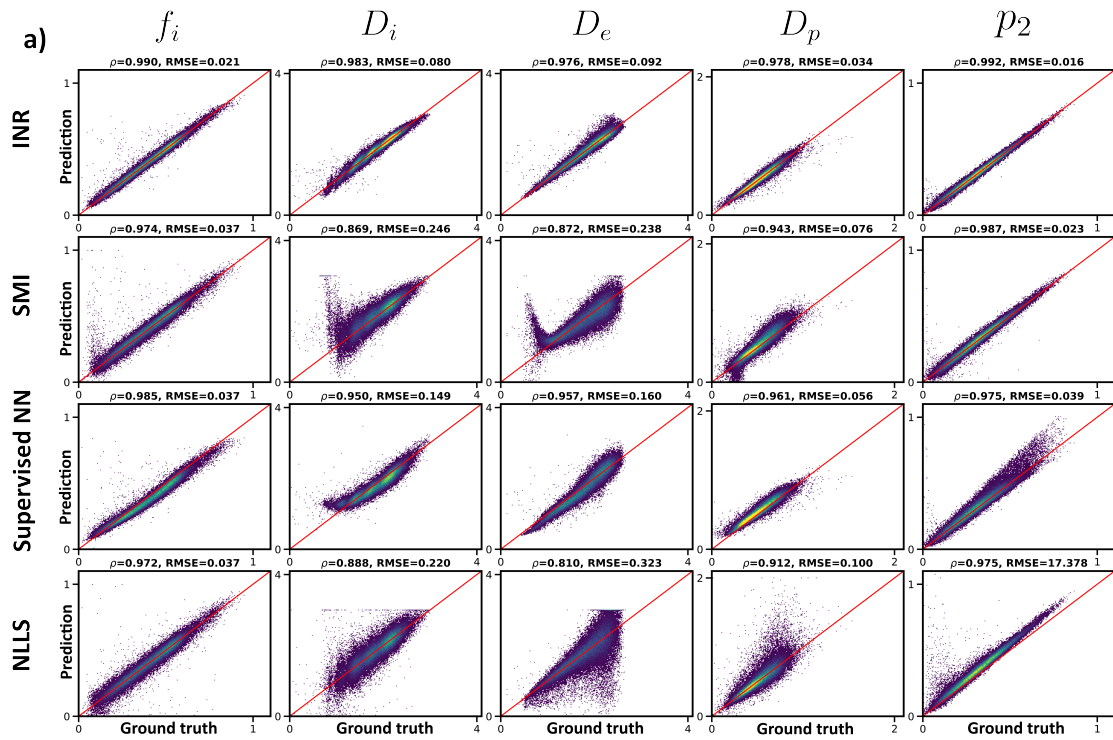


Figure B.11: Experiment 1 (SNR 50): **a)** Scatter density plots of the ground truth versus the parameter estimations of all methods. Row numbers correspond to method numbering from section 2.8.1. Title of the subplots indicate ρ and RMSE. **b)** SM parameter maps corresponding to the results in **a)**. Bottom row shows the ground truth (GT).

Appendix C. Rician loss SNR 50

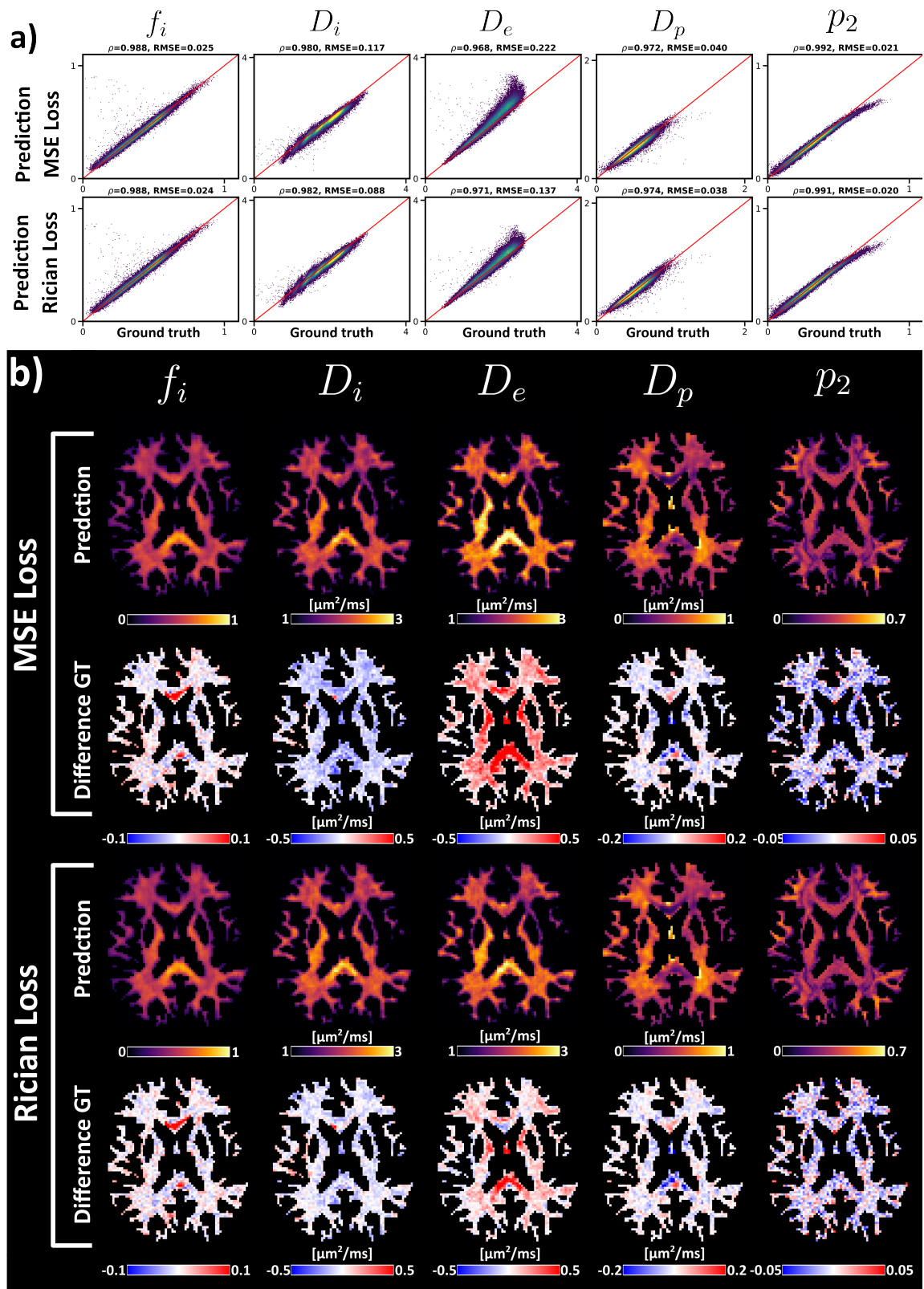


Figure C.12: Effect of Rician Loss Likelihood function (SNR = 50). **a)** Scatter plots for estimation with MSE and Rician loss. **b)** Brain parameter maps of the predictions from **a)**. Difference maps are with the ground truth parameters.

Appendix D. Parameter estimates for higher SH orders

To illustrate the difference in parameter estimates between different l_{max} values, we calculate the median absolute difference between parameter maps. For the synthetic datasets this is calculated between the ground truth parameter maps and the different SH order fits of the INR, the results of which are shown in Table D.4. Because there is no ground truth available for the real dataset, we compare the higher SH order estimates with the $l_{max} = 2$ fit. These results are shown in Table D.5. For both the synthetic and the real dataset there are no notable differences between the different SH order estimates. The noise robustness of the model is shown in the synthetic dataset, where the difference with the ground truth increases only slightly in the SNR = 50 dataset, compared to the noiseless one.

	l_{max}	Di	f	De	Dp	S0
Noiseless	2	0.034	0.006	0.046	0.015	0.728
	4	0.034	0.006	0.045	0.015	0.794
	6	0.034	0.006	0.044	0.014	0.629
	8	0.034	0.006	0.043	0.014	0.547
SNR = 50	2	0.047	0.011	0.051	0.019	1.628
	4	0.046	0.010	0.052	0.019	1.696
	6	0.046	0.010	0.051	0.019	1.855
	8	0.046	0.010	0.051	0.019	1.643

Table D.4: Table showing the median absolute differences between the ground truth and two synthetic dataset (noiseless and SNR = 50 gaussian noise) INR fits for different SH orders (l_{max}).

	l_{max}	Di	f	De	Dp	S0
Real	2	0.000	0.000	0.000	0.000	0.000
	4	0.016	0.005	0.022	0.011	5.725
	6	0.019	0.006	0.033	0.015	5.707
	8	0.018	0.006	0.033	0.015	4.419

Table D.5: Table showing the median absolute differences between the $l_{max} = 2$ INR fit for the real dataset and the higher SH order INR fits.